Universidad de los Andes

Faculty of Science

Physics Department

# Phenomenological Study of Heavy Neutrinos at the LHC Using the Vector Boson Fusion Technique

Author:

Carlos Miguel Patiño

Advisor: Carlos Andrés Flórez

Bogotá D.C.        2017

# Contents

# List of Figures

# Chapter 1

# Introduction

The standard model (SM) gathers the entire understanding about fundamental particles and their interactions. Although the model has successfully explained various physical phenomena observed experimentally, there are still multiple unanswered questions concerning particle physics. For example, experiments [1] have shown that accelerator and reactor, solar, and atmospheric neutrinos have mass by proving the existence of neutrino oscillations. The fact that there are neutrino oscillations contradicts the SM, because this model predicts that neutrinos are massless. Some specific experiments for each neutrino category are: Super-Kamiokande [2] for solar and atmospheric neutrino oscillations, KamLAND [3] for reactor neutrinos, and K2K [4] for accelerator neutrino oscillations [5]. An additional open question about neutrinos is the fact that only neutrinos with left helicity have been observed. Helicity is defined as the projection of the particle's momentum vector over its spin direction. If the spin of the particle is anto-parallel to its linear momentum, the particle has left helicity. Therefore, only neutrinos with spin anti-parallel to its linear momentum have been detected.

In order to provide neutrinos with mass, several theories that extend the predictions of the SM have been proposed. One of the most known models is the "see-saw" or balance mechanism [6]. This mechanism postulates the existence of a yet undetected particle called the heavy neutrino. In this model, the heavy neutrino would have a mass inversely proportional to the one of the neutrino. Since the current

experimental bounds on neutrino masses establish they have a considerably small mass, heavy neutrinos are expected to have large masses in the see-saw mechanism. Also, this neutrino would have a right helicity, which restores the right-left symmetry in the standard model. Other models that try to provide mass to the neutrinos by extending the SM postulate the conservation of the $(B - L)$ number, where $B$ is the baryon number and $L$ is the lepton number. Unlike these models, the see-saw mechanism proposes a breaking in the $(B - L)$ symmetry with consequences discussed in the next paragraph.

The see-saw mechanism includes three sub-models that provide mass to neutrinos. These three models come from the fact that is necessary to take into account the effects of breaking the $(B - L)$ symmetry. These effects can be parametrized using a Weinberg operator, and since there are only three ways in which this Weinberg operator can be obtained at tree-level, there are also three types of the see-saw mechanism [6]. The most common see-saw mechanism is the Type I and is described in further detail in Chapter 4. Taking into account the elements described above regarding the see-saw mechanism, if heavy neutrinos are observed, the left and right symmetry in the SM would be restored and the mechanism by which the neutrinos acquire mass would be explained.

Heavy neutrinos searches have been conducted in multiples experiments, but none has been able to prove that heavy neutrinos exist. Examples of these experiments can be found in collaborations such as LEP [7], CMS and ATLAS [8]. Searches at CMS and ATLAS have focused in final states with associated leptons and jets. However, these searches until now have not included the Vector Boson Fusion topology.

The main objective of this monograph is to perform a phenomenological study about the feasibility of conducting an experimental analysis for the detection of heavy neutrinos in the Large Hadron Collider (LHC) using a technique known as vector boson fusion (VBF). This technique has been recently used in the LHC [9] in searches for new physics. In high energy physics, the bosons $W^{\pm}$, $Z^0$ and $\gamma$ are known as vector bosons. The process of vector boson fusion occurs through an electroweak interaction of associated quarks with the LHC proton beams. The VBF topology consists in requiring two highly energetic jets in the longitundinal region of the detector and in opposite hemispheres thereof. It has

been shown that by requiring this type of event, the noise level (background) is reduced considerably in regions of difficult study in searches of new physics.

In order to conduct the analysis, it is important to simulate signal and background processes and to perform a detailed physical study of the variables that allow to distinguish signal from experimental noise. It is necessary to use a cuantitative estimator commonly known as figure of merit to determine optimal cuts in the mentioned variables. The latter with the objective of reducing the amount of experimental noise by finding the optimal cuts in the relevant variables. Furthermore, it is important to establish the expected experimental sensitivity using maximum likelihood limits or the calculation of the final significance for different hypothetical signal points. The procedure described would allow to conclude whether a study for the detection of heavy neutrinos at the LHC is feasible or not.

# Chapter 2

# Objectives

## 2.1 General Objectives

Conduct a phenomenological study to determine the possible experimental sensitivity of heavy neutrino searches in the LHC, using the VBF topology, in channels with high-mass resonance production.

## 2.2 Specific Objectives

- Develop the signal events and experimental noise simulations using MadGraph, Pythia, and Delphes software.

- Write an analysis code using ROOT software to analyze the simulated data.

- Conduct a physical study of the appropiate cinematic and topological variables that show strong separation between signal and background.

- Find the optimal cut points of the relevant physical variables using a significance figure.

- Conduct a statical analysis of the results.

# Chapter 3

# Definitions

## 3.1  Jet

A jet can be considered as a collimated spray of stable particles that arises from the fragmentation and hadronization of a quark or a gluon [10]. Since a jet is a shower of particles, algorithms of reconstruction have to be defined to gather all the information from the shower and define a jet as single element observed in the detector. The most common algorithms that define jets assume that the particle shower will arrive in a conical region in the detector. Hence, these algorithms establish a cluster in the $\eta - \phi$ space that defines where all the particles that make up the jet would arrive.

A schematic description of the production and definition of a jet is presented in Figure 3.1. The diagram shows how, as a result from the proton-proton collision, gluons and quarks are generated. Then, as described later in Section 7.1, the partons hadronize resulting in stable particles that are then observed in the detector. It can be seen in the figure the importance of defining correctly the cone of the jet. If the cone radius is too small, some particles that came from the initial parton may be left out, but if the radius is too large some particles that came from a different parton can be mistaken as part of the jet.
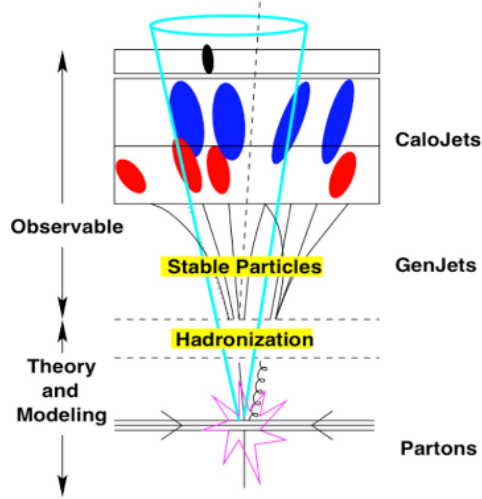
Figure 3.1: Schematic diagram of the creation and definition of a jet. (Taken from [10])

Variations of the cone algorithms are defined to gain more precision in the jet definition. Being able to reconstruct correctly all the particles making up the jet is important, because the jet provides a link between the observed particles in the detector and the physics at the partonic level [10]. In other words, since gluons and quarks decay rapidly, the only way to obtain information in detectors about processes related to partons are through jets. This is why more sophisticated algorithms to fully reconstruct jets in detectors and simulations are developed. For example, the iterative cone with progressive removal algorithm, or IC-PR algorithm, is used in CMS and the software Pythia [10]. The algorithm starts by finding the cell in the detector with largest transverse momentum and makes it a seed. Then, a cone is defined around the seed and a trial jet axis is calculated. If the trial jet axis is the same as the axis of the cone defined from the seed, then the cone is labelled as stable and all the particles that lie inside the cone are defined as the jet. If the trial jet axis does not equal the seed axis, the trial jet axis is defined as the new seed axis. The process described above is repeated until a

convergence of the axes occurs. This algorithm is repeated until there are no seeds above a threshold energy left [10].

## 3.2 Variable Definitions

The transverse momentum or $p_T$, is defined as the momentum component that a particle has in the plane perpendicular to the beam line. In the coordinate system of the LHC, the transverse plane corresponds to the $x - y$ plane.

The variable related with the polar angle in the LHC is called pseudorapidity, or $\eta$, defined as in Equation 3.1. The use of this variable is justified for mainly two reasons. The first one is that $\Delta\eta$, contrary to $\Delta\theta$, is a Lorentz invariant. This makes $\Delta\eta$ a more natural variable than $\Delta\theta$ for relativistic calculations. The second reason is that the distribution of the values of $\eta$ in the barrel region, where the multiplicity of particle is less than in the end-caps, is wider, allowing $\eta$ to have a more uniform particle number distribution.

$$\eta = -\ln\left[\tan\left(\frac{\theta}{2}\right)\right] \tag{3.1}$$

Sometimes it is necessary to determine the total angular separation between two particle in the detector, that is, determining the separation in both $\phi$ and $\eta$. This is accomplished using the variable $\Delta R$, defined in Equation 3.2. As stated earlier, it is generally used to determine how close in the detector two particles are. Taking this into account, $\Delta R$ is useful to establish whether two particles may have overlapped detection points in the detector.

$$\Delta R = \sqrt{(\Delta\eta)^2 + (\Delta\phi)^2} \tag{3.2}$$

Another useful variable defined in particle physics is the missing transverse energy or $\not{E}_T$. Given that the protons in the LHC collide along the $z$ axis, the initial momentum in the $x$ and $y$ components is zero. Since momentum in all directions must be conserved during the collision, the momentum after the collision must also be zero. However, there are particles resulting from the proton-proton collision, such as the

neutrinos, that cannot be observed by the components in the detector. That is why the energy corresponding to these unobserved particles is going to be missing from the energy observed in the detector. Considering what has been said in this paragraph, the momentum equation in the $x - y$ plane must be

$$\sum_{i=1}^{m} p_T(i)^{observed} + \sum_{j=1}^{n} p_T(i)^{missing} = 0$$

Taking the last equation into account, it is natural to define the missing transverse energy as the negative sum of transverse momenta of the observed particles in the detector. This definition is presented in Equation 3.3.

$$\not{E}_T = -\sum_{i=1}^{m} p_T(i)^{observed} \tag{3.3}$$

With the idea of exploiting the possible difference between signal and background in the $p_T$ for jets and $\tau$'s, two new variables shown in Equations 3.4 and 3.5 were defined to check for possible further separation between signal and background. As shown in equation 3.4, the $H_T$ variable is defined as the scalar sum of the jets in the event that are not B-jets. $S_T$ is defined as the scalar sum of jets that fullfilll the same conditions of $H_T$, added to the $p_T$ of the $\tau$'s in the event.

$$H_T = \sum_{i=1}^{n} p_T(jet_i) \tag{3.4}$$

$$S_T = \sum_{i=1}^{n} p_T(jet_i) + \sum_{j=1}^{m} p_T(\tau_j) \tag{3.5}$$

Another variable that turned out to be useful in the analysis is the transverse mass between the $\tau$ and the $\not{E}_T$ defined in Equation 3.6. In this equation, $\phi_{\tau,\not{E}_T}$ is the angle between the two vectors in the $x - y$ plane, i.e. the transverse plane in the detector. The definition shown of transverse mass can be obtained from 4-momentum conservation and

assuming that the transverse momentum of the tau is much greater that the missing transverse energy in the event.

$$m_T = \sqrt{2|\vec{p}_T(\tau)||\vec{\rlap{E}}_T|(1 - \cos(\phi_{\tau,\rlap{E}_T}))} \tag{3.6}$$

Throughout the analysis it is important to establish a cuantitative estimator to define the amount of signal compared to the amount of background. For that purpose, a cuantitative estimator, commonly known as figure of merit, is used to determine optimal cuts in the relevant variables. This figure of merit allows to find the optimal cuts in the relevant variables by giving a cuantitative result of the amount of signal events compared to the number of background events. For this particular analysis, the significance formula that was used is the one shown in Equation 3.7, where $S$ is the significance, $N(s)$ is the number of signal events, and $N(B)$ is the number of background events.

$$S = \frac{N(s)}{\sqrt{N(s) + N(B)}} \tag{3.7}$$

# Chapter 4

# The Neutrino Mass

The Standard Model predicts that the neutrino is a massless particle. However, experiments like the ones mentioned in Chapter 1 have proven that neutrino oscillations exist. These oscillations, contrary to the predictions of the SM, show that neutrinos are particles with mass. In this chapter, the mechanisms by which neutrinos can acquire mass in the SM are presented, followed by the reasons that do not allow to add mass to the neutrinos in the SM. Also, the see-saw mechanism is described in greater detail.

## 4.1   The L and B symmetries

The baryon number was first suggested by Ernst Stueckelberg in 1938 to explain why the proton does not decay into a positron and a gamma ray [11]. Stueckelberg assigned a baryon number of $B = 1$ to the proton and the neutron and $B = -1$ to the antiproton and antineutron. Leptons, photons, and mesons are assigned $B = 0$. The definition of the baryon number was later generalized to be as the one shown in Equation 4.1, where $n_q$ is the number of quarks and $n_{\bar{q}}$ is the number of antiquarks.

$$B = \frac{1}{3} \left( n_q - n_{\bar{q}} \right) \tag{4.1}$$

The baryon number conservation states that the baryon number in a process must be conserved, i.e. $\sum B = \text{const.}$  This conservation law

can arise more formally from the global gauge transformation shown in Equation 4.2 [11].

$$\psi' = \psi e^{i\epsilon B} \tag{4.2}$$

In 1953, E. J. Konopinski and H.M. Mahmoud introduced the lepton number $L$. They assigned $L = 1$ to $e^-$, $\mu^-$, $\nu_e$ and $\nu_\mu$, $L = -1$ to the antileptons, and $L = 0$ to all the other particles. This lepton number was later generalized to the $\tau$ and the $\nu_\tau$. The lepton number conservation, as the baryon number conservation, can also arise from a global gauge transformation like the one shown in Equation 4.3 [11].

$$\psi' = \psi e^{i\epsilon L} \tag{4.3}$$

## 4.2 The Dirac Mass

A standar Dirac free fermion can be described using the Langrangian shown is Equation 4.4 [12], where $\partial\!\!\!/ = \gamma^\mu \partial_\mu$ and $m$ is the mass of the particle. Since the mass term in this Langragian is $-m\bar{\psi}\psi$, a mass term of this form is always called a Dirac mass term. The best known description for a neutrino is the a neutral standard Dirac particle. That is, a neutrino can be described by the Langrangian showed in Equation 4.4, where $\psi$ would be a four component Dirac field describing the neutrino, generally defined as $\nu$.

$$\mathcal{L} = \overline{\psi} \left( i\partial\!\!\!/ - m \right) \psi \tag{4.4}$$

If the field $\psi$ is decomposed into the corresponding left and right chiral states, the Dirac mass term can be written as

$$-m(\overline{\psi_L + \psi_R})(\psi_L + \psi_R)$$

As shown in Appendix A, the terms $\bar{\psi}_R \psi_R$ and $\overline{\psi}_L \psi_L$ are zero. Therefore, the Dirac mass term can be written as shown in Equation 4.5.

$$- m \left( \overline{\psi}_L \psi_R + \overline{\psi}_R \psi_L \right) \tag{4.5}$$

For the particular case of the neutrinos, and taking into account the three neutrino flavors or generations, $\psi_L$ and $\psi_R$ would correspond to the $\nu_L$ and $\nu_R$ shown in Equation 4.6 [12].

$$\nu_L = \begin{pmatrix} \nu_e \\ \nu_\mu \\ \nu_\tau \end{pmatrix}_L , \quad \nu_R = \begin{pmatrix} \nu_e \\ \nu_\mu \\ \nu_\tau \end{pmatrix}_R \tag{4.6}$$

In the generalization for the three neutrino generations, the Dirac mass Lagrangian, or Dirac mass term, is like the one shown in Equation 4.7. The matrix $\mathcal{M}_D$ is in general a $3\times3$ complex mass matrix [12]. This matrix would contain the mass values corresponding to a Dirac coupling of the neutrinos if a neutrino with right helicity existed. These values, analogous to the mass matrices for the leptons, would be determined by the electroweak interaction.

$$\mathcal{L}^D_{mass} = -\left(\bar{\nu}_R \mathcal{M}_D \nu_L + \bar{\nu}_L \mathcal{M}_D \nu_R\right) \tag{4.7}$$

## 4.3   The Majorana Mass

The Majorana neutrino ($\nu_M$) is a neutrino proposed by Majorana in 1937 that satisfies the property shown in Equation 4.8, where $\mathbf{C}$ is the charge conjugation operator [12]. This charge conjugation operator transforms a free neutrino state into an anti-neutrino state. Taking the latter into account, Equation 4.8 implies that the Majorana neutrino is its own anti-particle.

$$\nu_M = \nu_M^C \equiv \mathbf{C}\nu_M\mathbf{C}^{-1} \tag{4.8}$$

As in the case of a Dirac fermion, a Lagrangian like the shown in Equation 4.9 can be defined. The factor $1/2$ is added to take into account double counting when an interaction term is added to the Lagrangian.

$$\mathcal{L} = \frac{1}{2}\bar{\nu}_M\left(i\slashed{\partial} - m\right)\nu_M \tag{4.9}$$

Once a neutrino that is its own anti-particle is defined, additional terms of the form $\overline{\nu^C}\nu^C$, $\overline{\nu^C}\nu$, and $\bar{\nu}\nu^C$ can be added to the mass term

shown in Equation 4.5 [12]. The addition of these terms does not violate charge conservation, because neutrinos are neutral particles. Hence, the Lorentz invariance in the Lagrangian is being conserved. The term $\overline{\nu^C}\nu^C$ is identical to $\overline{\nu}\nu$ except for an irrelevant surface term, so it would not be necessary to include it in the mass term in Equation 4.5 [12]. However, the other two terms mentioned above are not included in this mass term, so they should be added to the general mass Lagrangian. These two new mass terms, taking into account an hypothetical neutrino with right helicity, would be like the ones shown in Equations 4.10 and 4.11 where $m_L$ and $m_R$ are analogous to the mass in the Dirac mass Lagrangian. However, since these terms are not bounded yet by a theory, like the electroweak interaction for the value of $m_D$, in principle $m_L$ and $m_R$ do not have defined values. Nevertheless, for reasons described later in Section 4.5, these mass terms are assumed to have certain values.

$$\mathcal{L} \sim m_L \left( \overline{\nu_L^C}\nu_L + \overline{\nu}_L\nu_L^C \right) \tag{4.10}$$

$$\mathcal{L} \sim m_R \left( \overline{\nu_R^C}\nu_R + \overline{\nu}_R\nu_R^C \right) \tag{4.11}$$

If a Majorana neutrino is constructed as $\nu_M \equiv \nu_L + \nu_L^C$, Equation 4.10 can be written like in Equation 4.12. A similar definition can be made with an hypothetical neutrino with right helicity, so Equation 4.11 can also be written as 4.12. As in the Dirac case, Equation 4.12 is defined as the Majorana mass term. However, contrary to the Dirac mass term, the Majorana mass term can be constructed using either only $\nu_L$ or $\nu_R$ [12].

$$\mathcal{L} \sim m\overline{\nu}_M\nu_M \tag{4.12}$$

The Lagrangians shown in Equations 4.10 and 4.11 are valid for only one neutrino flavor. If the mass Lagrangian is generalized to the three neutrino generations as in the Dirac case, the Majorana mass Lagrangian would be the one shown in Equation 4.13. In this equation, h.c. stands for the hermitian conjugate of the other term in the Lagrangian and $\nu_L$ is the same as the one defined in Equation 4.6. As in the Dirac case, $\mathcal{M}_M$ is, in general, a complex $3 \times 3$ matrix with the additional property that this matrix is always symmetric, i.e. $\mathcal{M}_M = \mathcal{M}_M^\mathsf{T}$ [12].

$$\mathcal{L}^M_{mass} = -\frac{1}{2}\overline{\nu^C_L}\mathcal{M}_M\nu_L + \text{h.c} \tag{4.13}$$

## 4.4 Neutrino Mass in the Standard Model

As mentioned in Chapter 1, the Standard Model only includes a neutrino with left chirality. As shown in Equation 4.5, the abscence of a neutrino with right chirality makes that all the terms in the Dirac mass Lagrangian vanish. Therefore, it is not possible to add mass to the neutrinos in the Standard Model using a Dirac mass term.

Another mechanism that could provide mass to the neutrino in the Standard Model is the Majorana mass term. However, this term would not conserve the Lepton number, i.e. would violate the L symmetry, that is conserved throughout the Standard Model[13]. This happens because the Majorana fermions, in this case neutrinos, are their own antiparticles. A lepton number of $L = +1$ is assigned to a fermion and $L = -1$ to its antiparticle. Since the Majorana neutrinos are their own antiparticles, they do not have a well defined lepton number (it could be either +1 or -1). That is why the lepton number for both Majorana neutrinos would be either $L = 1$ or $L = -1$, so the Majorana mass term would violate de lepton conservation number by $\Delta L = \pm 2$. Also, some non-pertubative effects in the Standard Model can violate L symmetry but conserve the current $B - L$, where $B$ is the baryon number. To summarize, since the Majorana terms violate both $B - L$ and $L$ symmetries, these terms can not be used to introduced mass in the Standard Model using perturbation theory or non-perturbative effects [13].

Since these two mechanisms are not useful to explain the origin of the neutrino mass inside the Standard Model, a minimal extension to the SM is proposed in order to provide the neutrinos with mass. This extension consists in inserting right handed neutrinos to the model to explain the origin of the neutrino mass. In principle, the addition of this right handed neutrino would make the Dirac mass term different from zero, and the neutrino mass would be of the form of the charged leptons. Since the the mass terms of the leptons is of the form $m = Yv/\sqrt{2}$,

where $Y$ is the Yukawa coupling constant, this constant is required to be $Y \simeq 10^{-11}$ or less to explain the small mass of the neutrino. Given that the introduction of such a small coupling would require a symmetry reason for the small value, only introducing the right handed neutrino would not solve entirely the neutrino mass problem [14]. That is why an introduction of a model that explains both the neutrino mass and its small value must be introduced.

## 4.5   The See-Saw Mechanism

The See-Saw mechanism assumes the existance of a neutrino with right helicity. With this right-handed neutrino, and reminding that adding Majorana mass terms to the Lagrangian does not violate charge conservation, the most general mass Lagrangian would include Dirac and Majorana terms. Combining the Dirac and Majorana neutrinos mass terms discussed in the previous sections, the resulting mass Lagrangian would be the one shown in Equation 4.14, where $m_D$ is a Dirac mass, $m_L$ and $m_R$ are Majorana masses, and h.c is the hermitian conjugate.

$$\mathcal{L}_{mass} = -m_D \bar{\nu}_L \nu_R - \frac{1}{2} \left( m_L \overline{\nu^C}_L \nu_L + m_R \overline{\nu^C}_R \nu_R \right) + \text{h.c} \qquad (4.14)$$

If the vector $\nu$ is defined as

$$\nu \equiv \begin{pmatrix} \nu_L \\ \nu_R^C \end{pmatrix},$$

then the Lagrangian in Equation 4.14 can be written as in Equation 4.15, where $\mathcal{M}$ is defined in Equation 4.16.

$$\mathcal{L}_{mass} = -\frac{1}{2} \overline{\nu^C} \mathcal{M} \nu + h.c \qquad (4.15)$$

$$\mathcal{M} = \begin{pmatrix} m_L & m_D \\ m_D & m_R \end{pmatrix} \qquad (4.16)$$

If matrix $\mathcal{M}$ is diagonalized, the two left handed neutrino mass eigenstates for the Majorana neutrinos, $\nu_1$ and $\nu_2$, can be expressed as in

Equation 4.17, where $\theta$ is the mixing angle. A more detailed calculation of the mass eigenstate Majorana neutrinos, can be found in Appendix B.

$$\nu_L = \nu_1 \cos\theta + \nu_2 \sin\theta$$
$$\nu_R^C = -\nu_1 \sin\theta + \nu_2 \cos\theta$$

or

$$\nu_1 = \nu_L \cos\theta - \nu_R^C \sin\theta$$
$$\nu_2 = \nu_L \sin\theta + \nu_R^C \cos\theta \tag{4.17}$$

To guarantee that the mass eigenvalues are positive, and insertion of $i$, the imaginary number, in the equation for $\nu_1$ in Equation 4.17 is necessary. With this insertion, $\nu_1$ would now be defined as

$$\nu_1 = i\nu_L \cos\theta - i\nu_R^C \sin\theta$$

Using the calculations performed in Appendix B, the mixing angle value would be the one shown in Equation 4.18, and the two mass eigenvalues would be the ones shown in Equation 4.19 [12].

$$\tan 2\theta = \frac{2m_D}{m_R - m_L} \tag{4.18}$$

$$m_1 = \frac{1}{2}\sqrt{4m_D^2 + (m_R - m_L)^2} - \frac{m_R + m_L}{2}$$
$$m_2 = \frac{1}{2}\sqrt{4m_D^2 + (m_R - m_L)^2} + \frac{m_R + m_L}{2} \tag{4.19}$$

The values of $m_D$, $m_R$, and $m_L$ for the see-saw mechanism are values in which $m_R$ is much larger than $m_D$ and $m_L$. That is, $m_R \gg m_D, m_L$. Furthermore, the value of $m_L$, the term of the left-handed Majorana neutrino, is chosen to be zero. The latter with the objective of leaving the standard weak interaction theory unchanged, since $m_L \neq 0$ would imply the addition of a left Majorana neutrino. Setting $m_L = 0$ and

making the approximation $m_R \gg m_D$ in Equation 4.19, the values for $m_1$ and $m_2$ are the ones shown in Equation 4.20. On one hand, it can be seen from Equation 4.20 that if $m_R$ has a large value, $m_2$ would also have a large value. On the other hand, if $m_R$ has a large value, $m_1$ has a small value. Because of this inverse proportionality between $m_1$ and $m_2$ this mechanism is called the see-saw mechanism. Also, and more important, since these eigenvalues are the ones that are actually observed in measurements, the see-saw mechanism would successfully explain the origin of the neutrino mass as well as the small values for the neutrino mass observed in experiments. In this mechanism, $m_D$ is the mass scale associated with the SM, whereas $m_R$ is the scale provided by models beyond the SM [12]. It is also noteworthy that for the values of $m_R$ and $m_D$ considered, the mixing angle approaches to zero. This fact indicates that the eigenstates $\nu_1$ and $\nu_2$ would be completely decoupled.

$$m_1 \simeq \frac{m_D^2}{m_R}, \quad m_2 \simeq m_R \tag{4.20}$$

To end the study of the see-saw mechanism, it is worth mentioning that the analysis followed in this section was for only one neutrino flavor. Firstly, Equation 4.20 would turn into the expression in Equation 4.21, where each of the elements is a $3 \times 3$ matrix. Also, the matrix in Equation 4.16, in the case of three neutrino generations, would be the one shown in Equation 4.22 where each of the elements in the matrix is a $3 \times 3$ matrix [12].

$$m_1 = m_D \frac{1}{m_R} m_D^{\intercal} \tag{4.21}$$

$$\mathcal{M}_6(6 \times 6) = \begin{pmatrix} 0 & m_D \\ m_D^{\intercal} & \mathcal{M}_3 \end{pmatrix} \tag{4.22}$$

If the matrix in 4.22 is diagonalized by blocks and if the mixings between flavors are neglected, a term for the neutrino masses in each generation like the one in Equation 4.23 would be obtained with $m_{f,i} = (m_e, m_\mu, m_\tau)$. In the process of obtaining Equation 4.23, $\mathcal{M}_3$ is assumed to be of the form shown in Equation 4.24.

$$m(\nu_i) \simeq \frac{m_{f,i}^2}{M_R} \tag{4.23}$$

$$\mathcal{M}_3 \simeq M_R \begin{pmatrix} 1 & 0 & 0 \\ 0 & 1 & 0 \\ 0 & 0 & 1 \end{pmatrix} \tag{4.24}$$

However, it is also possible that the eigenvalues of are not all $M_R$ as in Equation 4.23, but $M_1$, $M_2$, and $M_3$. This difference in the eigenvalues would lead to a similar hierarchy to the one observed in the charged lepton masses [12].

As a final note, due to the inclusion of Majorana mass terms in the mechanism, and as stated earlier in this chapter, a breaking of the $L$ symmetry is induced in the see-saw mechanism. Nevertheless, this does not rises a problem for the validity of the see-saw mechanism since the energy scales of the heavy neutrino, scales at which the $L$ symmetry would break, would be very large. These large scales have not been yet reached by the particle physics experiments, so that would explain the lack of experimental evidence of the breaking of the $L$ symmetry.

# Chapter 5

# Heavy Neutrino Searches

## 5.1   Neutrino Searches in the LHC

Heavy neutrino searches in the LHC have mainly focused in production via Drell-Yan mechanism. The Feynman diagram for this process is shown in Figure 5.2. As shown in the diagram, the heavy neutrino results from a W boson that decays into a lepton and the heavy neutrino. In this model, the heavy neutrino decays into a lepton and a W boson. The latter decays into two quarks that result in two jets observed by the detector. Advances in the collision energies provided by the LHC have allowed probing for masses of heavy neutrino at larger scales. This fact is shown in Figure 5.1 where a comparison in the cross section of the Drell-Yan heavy neutrino process in the Tevatron and the LHC is shown. It can be seen clearly that the LHC, due to its higher center of mass energy in the collision, has a greater cross section than the one present at the Tevatron for the same process [15].
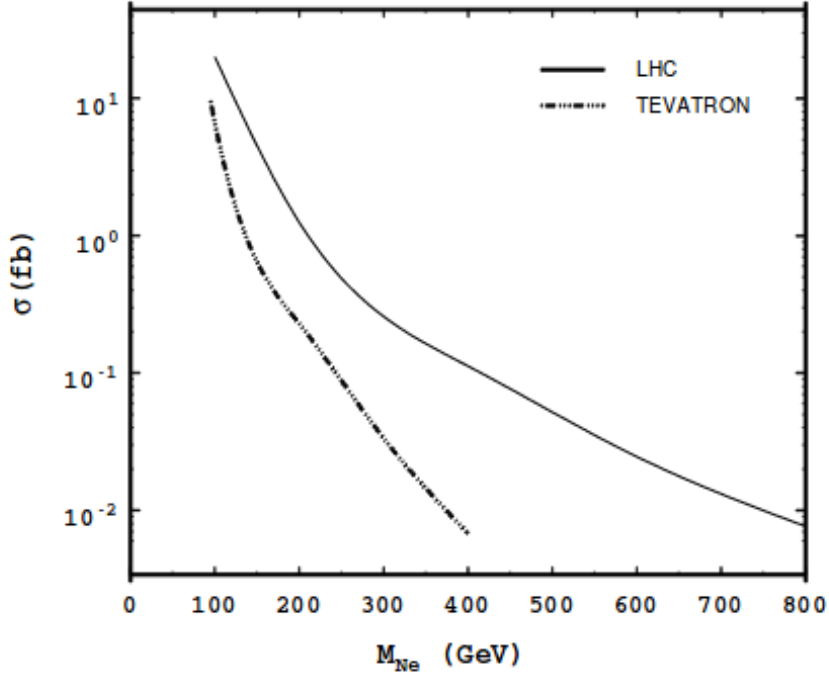
Figure 5.1: Cross sections for heavy neutrino production at the LHC and the Tevatron (Taken from [15])

As mentioned in [16], the process mentioned above is the dominant signal for a heavy neutrino with a mass between the 100 GeV and 500 GeV. The main problem with this type of process is that, given there is a W boson in the heavy neutrino production, the cross section for large values of the heavy neutrino mass decreases rapidly. The fast decrease in the signal cross section can be observed in Figure 5.1. This small cross section rises a problem to experimentally observe a signal with a heavy neutrino mass greater than 400 GeV [16].

Although the production of heavy neutrino through the Drell-Yan process has a small cross section, it has the advantage of having a clean

signal if the heavy neutrino has a decay of the form $N \to l^{\pm}W^{\mp} \to l^{\pm}jj$ [16]. This type of process allows the detection of all the products of the final state of the process. That is, signal from the two leptons and the two jets that result at the end of the process should be observed in the detector.
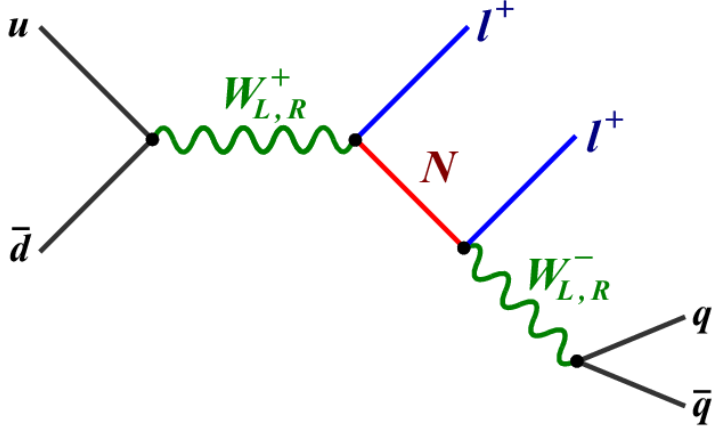


Figure 5.2: Feynman diagram of heavy neutrino production by Drell-Yan process

As noted in [6], all the heavy neutrino searches in the LHC have focused in the Drell-Yan process. It is also mentioned that studies involving final states with taus have not been explored because of the challenges of reconstructing and tagging correctly a $\tau$. However, it is also mentioned that this can be solved with the improvement of $\tau$-tagging algorithms. The latter makes a study like the one presented in this monograph novel, because of the inclusion of taus instead of muons and electrons in the final state.

## 5.2 Heavy Neutrino Search with Vector Boson Fusion

The first difference between most of the studies mentioned in the previous section and the one done in this study is the use of $\tau$ instead of $\mu$ for the lepton in the the process. The second, and main difference, is the use of the Vector Boson Fusion technique. As stated earlier, neutrino searches have been mainly performed using the Drell-Yan mechanism shown in Figure 5.2. However, a search using the Vector Boson Fusion, or VBF, technique has not been conducted. The main difference between the Drell-Yan process and the one including the VBF topology is the addition of two jets resulting from the fusion of two bosons. These two jets would have the characteristic of traveling in opposite directions and in the longitudinal region of the detector when they are created. As a result, the VBF topology includes two jets with a big angular separation in the detector, because they should be detected in opposite hemispheres (high $\Delta\eta$ separation) and in the endcap region (large $\eta$ values). Also, the jets coming from the Vector Boson Fusion process would typically have greater transverse momentum $p_T$ than jets coming from, for example, the quarks resulting from the decay of bosons. These characteristics mentioned above would allow to identify these jets coming from the VBF process, hence increasing the possibility of identifying the signal from experimental noise in the detector.

The addition of Vector Boson Fusion to the Drell-Yan process of the heavy neutrino would result in Feynman diagrams like the ones shown in Figures 5.3 and 5.4. Figure 5.3 shows the production of a heavy neutrino including the fusion of boson Z with boson W, and Figure 5.4 shows the fusion of boson gamma, or photon, with boson W. These two examples show that the bosons that fuse in the VBF processes can be multiple combinations of vector bosons. Also, it is noteworthy that the Feynman diagram portion regarding the production of the heavy neutrino remains unchanged compared to the one of the Drell-Yan production process shown in Figure 5.2. The latter shows how the Vector Boson Fusion is an addition to the process that would help with the identification of the signal, but does not affect the original process that is being studied. The final states for the processes shown in these two diagrams would

include two jets coming from the VBF process, two $\tau$'s, and two jets coming from the quarks resulting of the $W^-$ decay
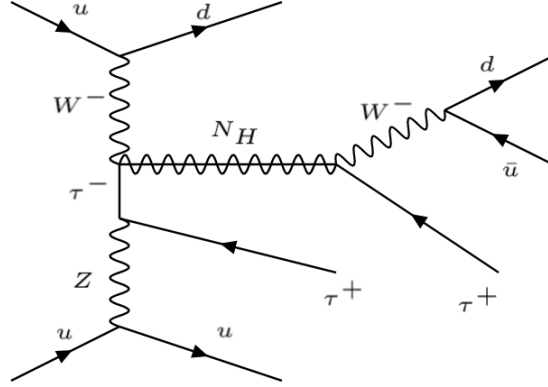


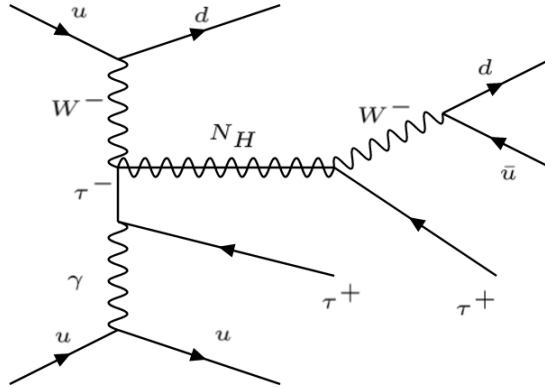Figure 5.3: Feynman diagram of heavy neutrino production including VBF and involving Z boson



Figure 5.4: Feynman diagram of heavy neutrino production including VBF and involving photon

A search using the VBF topology would be promising, because there could be a potential enhancement of the signal cross section compared with the heavy neutrino production via Drell-Yan process. A comparison of the cross section of both processes is shown in Figure 5.5. Although in both cases the cross section decreases when the mass of the heavy neutrino increases, the cross section of the VBF process decay is slower than the one of the Drell-Yan process. This causes that from a value for the heavy neutrino mass of approximately 1.4 TeV the VBF process has a greater cross section compared to the cross section of the heavy neutrino produced by the Drell-Yan process. This plot shows clearly why it is relevant to perform the analysis of a potential search of heavy neutrinos at the LHC using the Vector Boson Fusion technique. Furthermore, this new production model allows to study the couplings of heavy neutrinos to vector bosons. If couplings of heavy neutrinos to quarks are weak, this might be the only production mechanism available to detect heavy neutrinos. In addition, VBF allows a reduction in 3-4 orders of magnitude the presence of background events from Quantum-Chromo-Dynamic events, referred to as QCD. QCD events is one of the largest backgrounds in experimental searches with hadronically decaying taus.
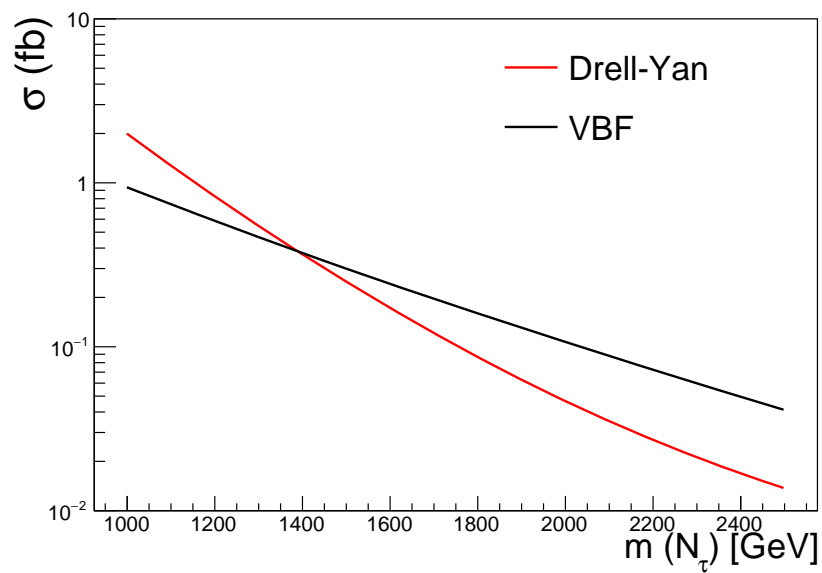
Figure 5.5: Feynman diagram of heavy neutrino production by Drell-Yan process

# Chapter 6

# Backgrounds

Backgrounds in particle physics experimental studies are processes that have similar final states to the process that is being studied. Because of their similar final states with the process of interest, background signal can be mistaken as the signal of the process being studied. That is why backgrounds are experimental noise that is not desirable in a study and that has to be eliminated as much as possible. In this particular study three backgrounds were considered because of their similarity in the final states with the one of the heavy neutrino production.

One of the backgrounds considered for this analysis was the W + jets process shown in Figure 6.1. This process is considered as a background for the heavy neutrino production because of the presence of one lepton coming from the decay of the W boson in the process. It can be noted that in principle this process would not have the second lepton present in the heavy neutrino production process. However, it is has to be remembered that taus are observed as jets in the detector. There is a possibility of tagging a jet as a tau incorrectly. Since the gluon, the quark $b$ and the other quarks present in the process are also observed in the detector as jets, these could by identified incorrectly as a tau. If one of these jets is tagged incorrectly, then the final state of the W + jets process would be the same as the one of the heavy neutrino process because it would be identified as a process with two leptons and two jets.
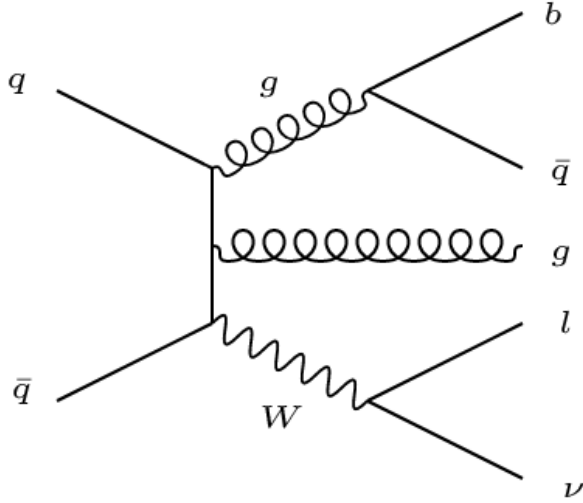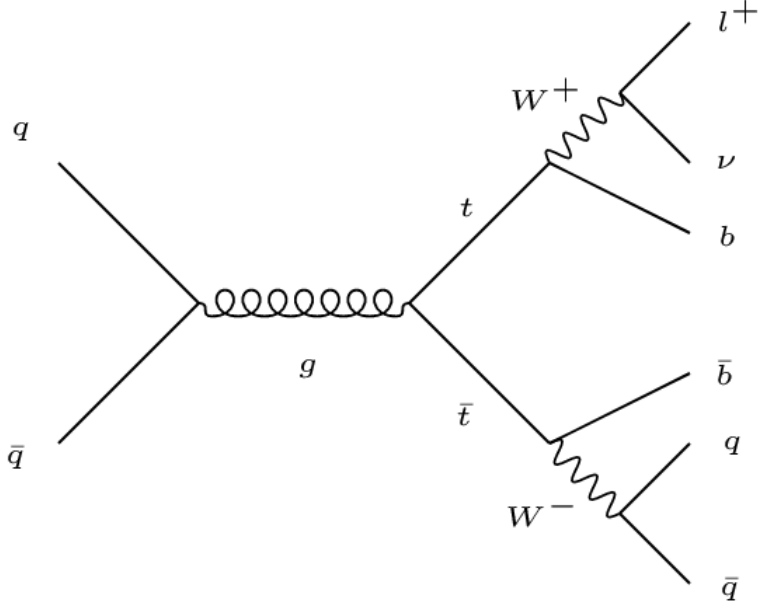
Figure 6.1: Feynman diagram of W+jets process

Another background considered was the $t\bar{t}$ semileptonic process that contains the decay of a gluon into the quarks top and anti-top as shown in Figure 6.2. This is the semileptonic $t\bar{t}$ process because while one top quark decays to a bottom quark and two jets, the other top quark decays into a bottom quark, a neutrino, and a lepton. This process has the chracteristic of having two B-jets, or jets coming from bottom quarks, in its final state.

Figure 6.2: Feynman diagram of $t\bar{t}$ process

The other background considered for the analysis is the Drell-Yan process shown in Figure 6.3. The reason for this process to be considered as a background is the two leptons in its final state as well as the two jets coming from the initial state radiation jets. It can be seen that from the three backgrounds, Drell-Yan is the one that is the most similar to the heavy neutrino production, because the heavy neutrino process considered for this analysis also has two jets and two leptons in the final state. This is why the Drell-Yan background was expected to be the most difficult to separate from the signal of interest in the analysis.
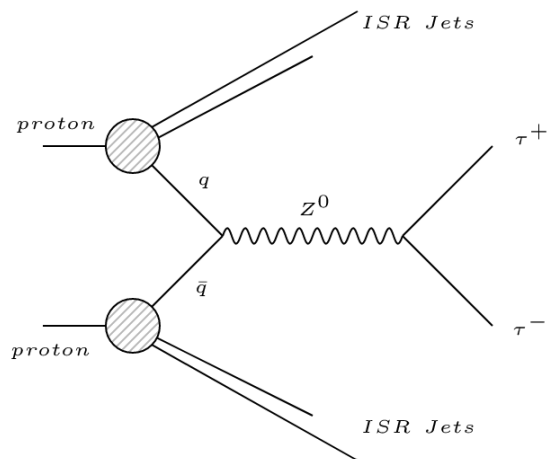
Figure 6.3: Feynman diagram of Drell-Yan process

# Chapter 7

# Signal Simulation and Analysis

## 7.1 Simulation Computational Resources

The project required computational work, because simulations of events from the different processes were needed. Also, an analysis of the samples using the analysis code was required. The background and signal samples were simulated using the software MadGraph [17], Pythia [18] and Delphes [19]. The data analysis and all the subsequent kinematic, topological, and optimal cuts analyses were performed using ROOT software [20].

MadGraph is an event generator software that allows the simulation of collision between two particle beams. For this analysis in particular, the simulations will consist in proton-proton collisions at 13 TeV in order to emulate the actual conditions of the LHC. MadGraph includes the physical parameters that determine the production probability of a given process, as well as the possible decays of the simulated particles. Besides providing the necessary matrices to calculate the cross sections of the processes, MadGraph also creates the pictorial representations of the Feynman Diagrams from the generated processes. To this end, the software uses perturbation theory in the calculations of production and generation of physical processes.

Pythia is a software that allows the simulation of various strong processes models that evolve from a few bodies to final states with high particle multiplicity. Particularly, in this case Pythia will be used for the simulation of quark and gluon fragmentation processes. This fragmentation process occurs when, due to and intrinsic characteristic of the strong interaction, there is an energy gain caused by the increase of the distance of two bound quarks. If the separation is enough to reach a critical energy, a pair quark-antiquark is created. The Pythia simulation is necessary, because processes like the ones mentioned above occur during a proton collision at the LHC.

Delphes is a software used to add to the simulation the effects that a multipurpose detector, like ATLAS or CMS, may have on the particles. In this particular case, Delphes is necessary to simulate the interaction of the particles coming from the generated processes in MadGraph and Pythia with the CMS components. Namely, reproducing the conditions of the detector and the uncertainties coming from the measuring process is achieved by using Delphes. The changes in the kinematic variables due to their interaction with matter, errors caused by the electronics of the detector, and the additional particles generated because of the interaction between the particles and the detector components can be accounted for using Delphes. Other functionalities included in Delphes are: simulation of the detector geometry, the effect of the magnetic field over the particles, and the particle identification and reconstruction efficiencies, among others.

## 7.2 Simulation Process

The MadGraph signal simulation was performed for six values of the heavy neutrino masses: 0.1, 0.5, 1.0, 1.25, 1.5, and 2.0 TeV. Also, taking into account that the analysis was going to be performed using VBF, the paramater of minimum pseudorapidity separation ($\Delta\eta$) between two jets was set to 3.5. This parameter allowed to have more events with the VBF topology in the simulation.

The commands used to generate the desired signal were the following:

- import model SM_HeavyN_NLO

- generate p p > n3 ta+ jj, QCD= 0, n3 > ta+ jj

- add process p p > n3 ta+ jj, QCD= 0, n3 > ta- jj

- add process p p > n3 ta- jj, QCD= 0, n3 > ta- jj

- add process p p > n3 ta- jj, QCD= 0, n3 > ta+ jj

The first command imports the theoretical model that includes the interactions related with the heavy neutrino formation and decay. The next command specifies the processes that are going to be simulated. pp > n3 ta+ jj stands por the proton-proton collision that decays into a heavy neutrino, a $\tau$ with positive charge, and two jets. The flag QCD=0 is used to exclude all strong interactions that can be involved in the process. Finally, n3 > ta+ jj is used to force the decay of the heavy neutrino into a $\tau$ charged positively and two jets. The subsequent commands are used to take into account all the possible combinations of the electrical charge that the $\tau$ may have. The additional parameter mentioned earlier of a separation greater than 3.5, i.e. $\Delta\eta > 3.5$, between VBF jets was included in run card of the simulation.

Each simulation was for 100,000 events. The simulation for the 1.5 TeV mass value was performed in 10 different simulation batches each one containing 10,000 events. Every batch was generated with a different random seed to guarantee the independence of the events between each one of the generated batches. This independence was necessary because the 10,000 event files were merged to form a single file with 100,000 events. The other three simulations were performed in a single run of 100,000 events each.

As explained earlier, after the events were simulated in MadGraph they were passed to Pythia and then to Delphes so the signal resembled one that could be found at a particle detector. Delphes has configuration cards that emulate the conditions of ATLAS and CMS. In our analysis, the card from CMS was used. The Pythia process using Pythia 6 and MadGraph 5 was done seamlessly, because Pythia 6 is intergrated directly into MadGraph 5. This functionality makes that to perform the

Pythia simulation process it is enough to turn on Pythia at the beginning of the MadGraph 5 simulation commands. To perform the Delphes simulation part, the output files from Pythia and MadGraph were used to execute a Delphes simulation.

## 7.3 Analysis Computational Resources

As mentioned earlier, the ROOT framework was used to perform all the analyses regarding kinematic and topological variables, and optimal cuts. ROOT is a software library developed by CERN to perform data analyses related with particle physics. One of the main characteristics of this library is the possibility of handling large volumes of data efficiently. The latter is achieved by using a tree structure in which the information related with the particles is stored and can be accessed easily using ROOT functionalities. Other features included in the library are the creation of histograms from data trees, multivariate analysis, four-vector calculations, among others. By using ROOT functionalities, it is also possible to estimate optimal cuts in variables to reduce experimental noise to its minimum. This is why the entire final analysis involved using tools provided by ROOT. A more detailed description of the analysis performed using ROOT is presented in the following chapters.

# Chapter 8

# Event Selection Criteria

## 8.1   Preselection Criteria

When an event is analyzed, several preselection criteria are established to count a signal observed in the detector as a valid particle. This is done to be certain that the signal received is indeed from the type of the particle that is expected. In this section, the preselection criteria used in this analysis are given. The summary of the criteria mentioned in this section is presented in Table 8.1.

In each event, a maximum of six jets that had a $p_T$ greater than 15 GeV and its absolute value of $\eta$ less than 5.0 were stored to be analyzed later. Among this list of jets, the two jets whose summed masses resulted in the greatest mass combination were stored and defined as the Di-Jet pair. The jet with greater momentum in the Di-Jet Pair is the leading jet and the other one in the pair is the sub-leading jet. These two jets are the ones related with the VBF process. Another variable defined regarding the Di-Jet Pair was the Di-Jet mass and corresponds to the sum of the masses from the jets in the Di-Jet Pair.

Since the $\tau$ selection is important for this analysis, it is relevant to provide a further description of the preselection criteria for the $\tau$'s in the simulated events. For starters, a jet identified as a tau is considered a valid $\tau$ if it has a transverse momentum greater than 20 GeV. Also, it was required that a valid $\tau$ should not overlap with an electron, a muon, or a jet. That is, the $\Delta R$, defined as in Equation 3.2, should not

| Variable | Criteria |
|----------|----------|
| $p_T(j)$ | > 40 GeV |
| $|\eta(j)|$ | < 5 |
| $p_T(\tau)$ | > 20 GeV |
| $p_T(j_B)$ | > 30 GeV |
| $\Delta R$ | > 0.3 |

Table 8.1: Preselection criteria table

be less than 0.3. This condition guarantees that the jet identified as a $\tau$ does not overlap with other leptons or jets. Since the final state for this analysis includes two $\tau$'s, the two taus with greater $p_T$ are selected among a maximum of three taus stored for each event. The leading $\tau$ is the one with highest $p_T$ and the sub-leading $\tau$ is the one with second highest $p_T$.

## 8.2   Variable Cut Optimization

To determine the optimal values for some of the variables, a study of the significance through multiple cuts was performed using the relation showed in Equation 3.7 for each cut value. The histograms analyzed were normalized to the luminosity, to emulate the accelerator performance, and to the corresponding cross section of the process to include the probability of production under the LHC conditions. Taking these parameters into account, the optimal cut values for the variables $\Delta\eta$ from the Di-Jet pair and the mass from the Di-Jet pair, $m(jj)$, was determined.

The result for the significance study for the $\Delta\eta$ from the Di-Jet pair is shown in Figure 8.1. The first cut value considered was 3.8, because, as mentioned earlier, it is expected that the jets from the VBF process have a big separation in $\eta$. It is clear from the plot in Figure 8.1 that the best value for the cut is 3.8. The significance for $\Delta\eta$ values greater than 3.8 tend to decrease. Figure 8.2 shows the signal significance as a function of Di-Jet mass. Note that the significance increases with mass. This significance increase is expected, because the production

of heavy neutrinos requires higher energies than average SM processes. Therefore, the jets involved in the VBF process have on average higher transverse momentum , which results in larger Di-Jet mass.
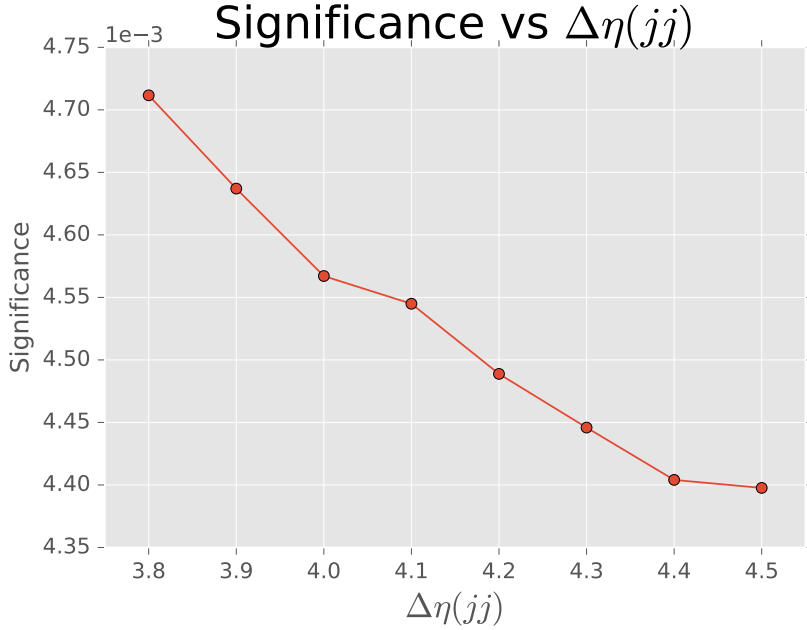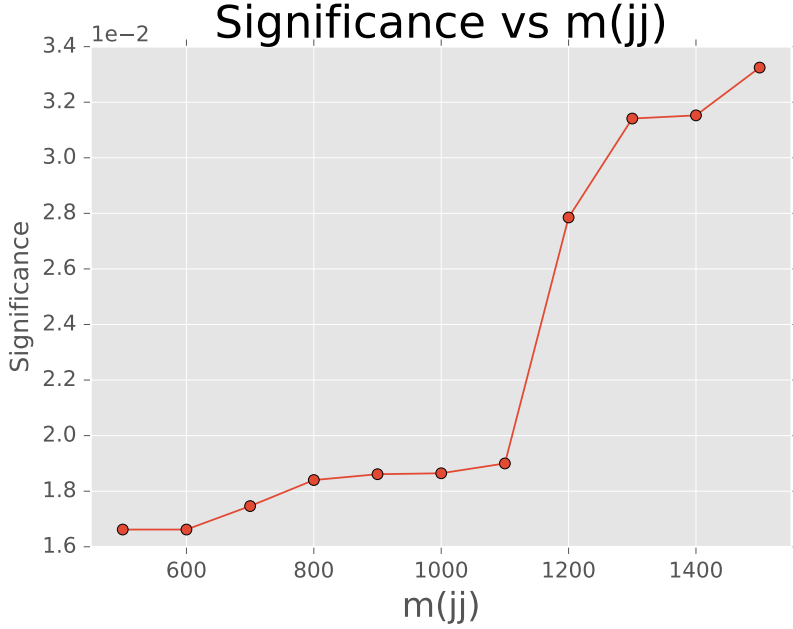


Figure 8.1: Significance of multiple cuts in $\Delta\eta$ diJet variable

The other variable analyzed using the figure of significance was the total mass of the Di-Jet Pair or $m(jj)$. The result of the significance is shown in Figure 8.2. It can be seen that the significance increases when the value for the cut in $m(jj)$ increases.

Figure 8.2: Significance of multiple cuts in $m(jj)$

## 8.3   Event Selection Criteria

In order to achieve a separation between background and signal, several successive requirements for the variables of the particles in the event were made. These requirements are defined as cuts, and for each cut the events that do not comply with the established condition are not taken into account to fill the histograms. Nine cuts were made to the histograms, storing in each cut the resulting distributions to analyze them later. The six cuts were related with jets and $\tau$'s in the event, and the subsequent three were related with the VBF topology. In the next paragraphs of this section a description of each one of the cuts is given as well as the order in which they were performed. A summary of the selection criteria can be found in Table 8.2.

The first cuts that were made to the histograms were to require that the leading and sub-leading $\tau$'s should have a minimum transverse

momentum of 50 GeV and 20 GeV respectively and a maximum of 2.1 for the absolute value of $\eta$. The latter guarantees that the $\tau$'s left are detected by the barrel and not the end-caps of the detector. That is an important condition because the detection components, such as the tracker, are in the barrel section and are more accurate than the ones in the end-caps. As a result, a signal detected in the barrel is most certain to be accurate than one detected in an end-cap.

The next cut requires that the event does not have any B-jet. This cut is justified by the fact that one of the main backgrounds for the signal is the top anti-top ($t\bar{t}$) process. The interaction bewteen the top and anti-top quark is related with the production of jets associated with the $b$ quark or B-jets. That is why, much of the $t\bar{t}$ should be eliminated by requiring no B-jets in the event. This fact will be later analized further in chapter 9. The cut that follows the one regarding the B-jets selects the events that have a minimum of two jets with transverse momentum greater than 40 GeV. This two jets must be different from the ones used in the Di-Jet Pair and are the ones that should result from the fragmentation of the quarks resulting of the W decay shown in Figure 5.2.

A selection criteria of requiring a combined mass of the two main taus in the event greater than 100 GeV was established. The case where there was only one leading tau in the event was analyzed so this selection criteria was not applied in that case. Also, it was required that the valid events had a missing transverse energy greater than 50 GeV.

The last three cuts made to the histograms are related to the VBF topology. The first of the three selects events in which the product of $\eta$ from the leading and sub-leading jets is negative. This condition guarantees that the jets in the Di-Jet Pair are in opposite hemispheres. The next cut requires that the leading and sub-leading jets of the event have a $\Delta\eta$ greater than 3.8. Finally, the last cut requires that the Di-Jet mass of the event is greater than 500 GeV.

| Variable | Criteria |
|----------|----------|
| $p_T(\tau_1)$ | $> 50$ GeV |
| $p_T(\tau_2)$ | $> 20$ GeV |
| $|\eta(\tau)|$ | $< 2.1$ |
| Number of B-jets | $= 0$ |
| $p_T(j)$ | $> 40$ GeV |
| Number of jets | $>= 2$ |
| $m(\tau_1, \tau_2)$ | $> 100$ GeV |
| $\not{E}_T$ | $> 50$ GeV |
| $\eta(j_l) \times \eta(j_s)$ | $< 0$ |
| $\Delta\eta(jj)$ | $> 3.8$ |
| $m(jj)$ | $> 500$ GeV |

Table 8.2: Selection criteria table

# Chapter 9

# Distribution Analysis

## 9.1 Normalized Distributions

The normalized plots are useful to check the shape of backgrounds and signal distributions. These shapes help to identify which variables are not useful for the analysis because the backgrounds overlap with the signal and which variables have to be studied with greater detail because the signal separates from the backgrounds from certain points. An example for both cases is provided in Figures 9.1 and 9.2. In figure 9.1 it can be seen that the signal overlaps for all values with the background distributions. That is why this plot can be used to conclude that the $\eta$ variable from the sub-leading $\tau$ is not useful to isolate the signal from the background. In contrast, the plot in Figure 9.2 show that from around 150 GeV the signal separates from the background distributions. This separation for the $p_T$ of the leading $\tau$ suggests that this variable should be examined more closely through the subsequent cuts.

To understand the definition of $H_T$ and $S_T$ mentioned in Chapter 3, the plots in Figure 9.3 are shown. The four plots show a separation, in some cases a smaller than others, between the signal and backgrounds distributions. A tendency of the signal jets to have greater transverse momentum than the ones in the backgrounds is shown. This tendency is also displayed for both $\tau$'s. Hence, the distributions of $H_T$ and $S_T$ should show a similar behaviour because these variables are the result

40
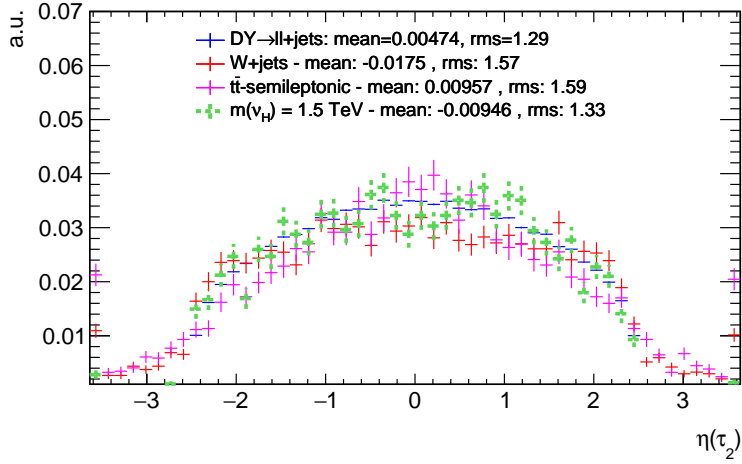
Figure 9.1: Unit plot of $\eta$ from the sub-leading $\tau$ with no cuts
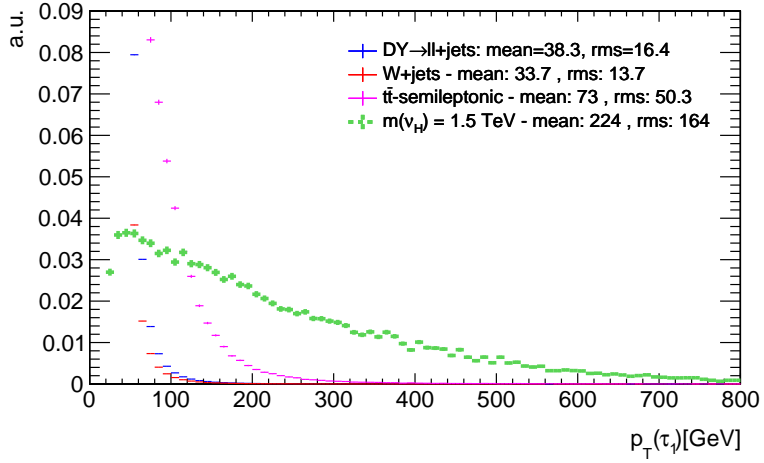


Figure 9.2: Unit plot of $p_T$ of leading $\tau$ with no cuts
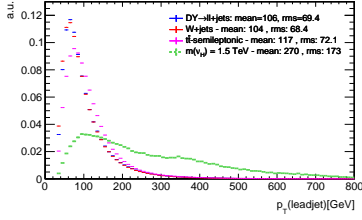
(a) Leading jet $p_T$ unit plot
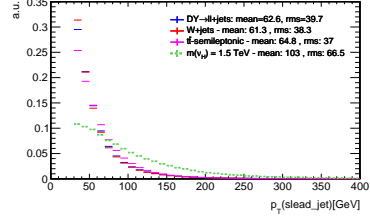


(b) Sub-leading jet $p_T$ unit plot
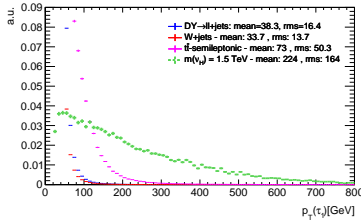


(c) Leading $\tau$ $p_T$ unit plot
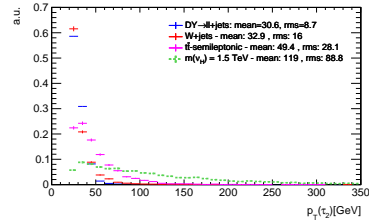


(d) Sub-leading $\tau$ $p_T$ unit plot

Figure 9.3: $p_T$ unit plots for different bodies in the event

of adding the transverse momentum of jets and $\tau$'s in the event.

In Figures 9.4 and 9.5, the normalized plots with no cuts of $H_T$ and $S_T$ are shown. It can be seen that indeed a greater separation between signal and background was achieved. Unlike the distributions of the $\tau$'s and jets transverse momentum, the maxima of $H_T$ and $S_T$ lie outside the backgrounds distributions. Furthermore, the background that overlaps at a greater energy with the signal corresponds to $t\bar{t}$. Taking into account what was mentioned in Section 8.3, the overlap between the signal and this background could be reduced with the cut related with the number of B-jets in the event. This is why these two variables need to be studied closer in the analysis.

Another variable relevant for the analysis was found out to be $m(jj)$. The reason for a further analysis of this variable is shown in Figure 9.6. As in the case of $H_T$ and $S_T$, the distribution of the mass of the Di-Jet pair shows a separation between the signal and the three backgrounds. Furthermore, it shows a greater separation than the one observed for
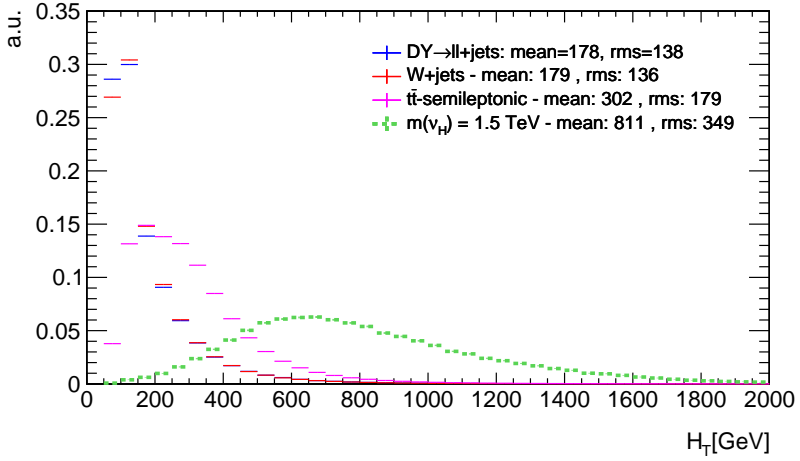
Figure 9.4: Unit plot of $H_T$ with no cuts
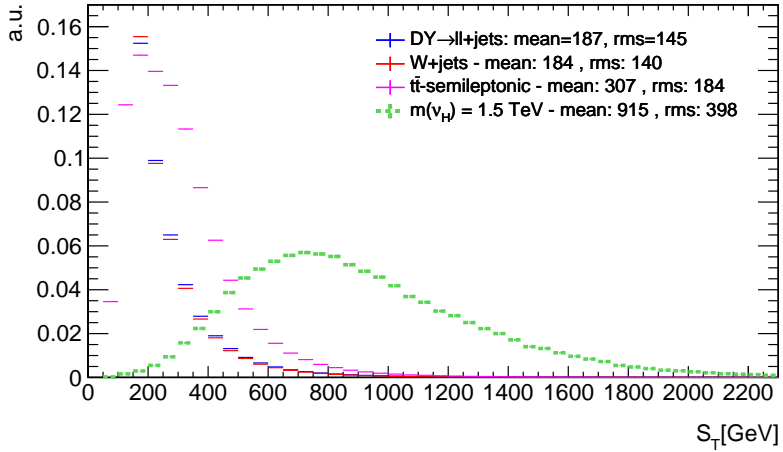


Figure 9.5: Unit plot of $S_T$ with no cuts
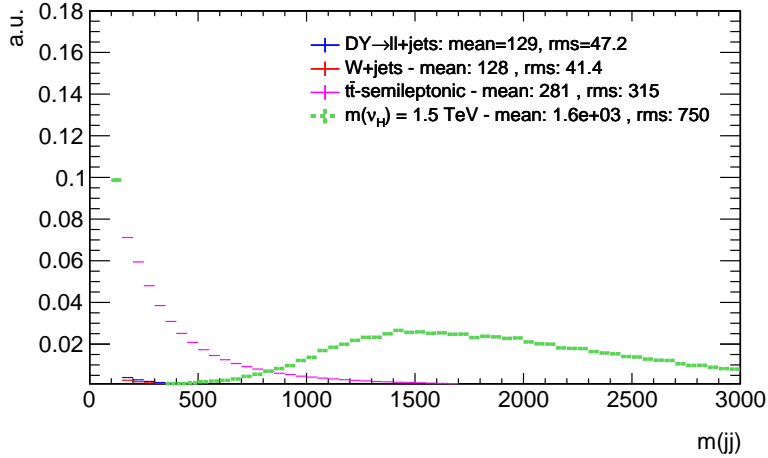
Figure 9.6: Unit plot of $m(jj)$ with no cuts

both $H_T$ and $S_T$. The variable $m(jj)$, or the total mass of the Di-Jet pair, has to be studied more closely, because it shows potential for a separation between signal and backgrounds.

## 9.2   Stacked Plots

The plots shown in this section are the ones corresponding with the relevant variables mentioned in section 9.1. All the plots presented are normalized to the cross section of each process and to a luminosity of $50 \text{ fb}^{-1}$. Also, since the amount of signal events is small after applying all the selection criteria, the number of events axis is in a logarithmic scale. This allows to examine the distribution shape more easily when the number of events of a distribution is small.

In Figures 9.7 and 9.8, the stacked plots for the $H_T$ distributions, with $\not{E}_T$ cuts of 50 and 60 GeV respectively, are shown. Comparing these two plots, it is observed that an increase of 10 GeV of the cut in the transverse missing energy is useful to separate the signal from the backgrounds. Focusing in the amount of background shown in Figures 9.7 and 9.8, it can be seen that with the increase in the $\not{E}_T$ cut,

the amount of background events was reduced from approximately 160 to about 40. Besides, with the new missing tranvserse energy cut, the amount of signal events was not significantly reduced. A similar conclusion can be drawn from Figures 9.9 through 9.12. The reduction in background resulting from this cut increase is mainly due to the fact of almost completely eliminating the W+jets background. Comparing the amount of W+jets in Figures 9.7, 9.9, and 9.11 with the amount present in Figures 9.8 and 9.10, and 9.12, it can be clearly seen that the background coming from W+jets is eliminated. It could be argued that a stronger cut in the missing transverse energy would increase the separation between signal and background. However, analyzing the $\not{E}_T$ distribution in 9.14, it can be seen that a further increase in the cut would also eliminate a considerable amount of signal events. The reasons presented in this paragraphs are why the increase of 10 GeV in the $\not{E}_T$ cut is convenient for separating signal from backgrounds.

As expected from the analysis performed in Section 9.1, the variables $H_T$ and $S_T$ show separation between signal and backgrounds. The latter can be observed in Figures 9.7 and 9.8 for $H_T$, and Figures 9.9 and 9.10 for $S_T$. However, from these four plots it can also be concluded that $S_T$ is a better variable than $H_T$ for this study. This conclusion can be drawn from the fact that the signal distribution decays slower in the $S_T$ variable than in $H_T$. These four plots required two taus in the event: the leading tau had a requirement of minimum transverse momentum of 50 GeV and the subleading tau a minimum $p_T$ of 20 GeV.

Although both $H_T$ and $S_T$ allow to obtain a separation between signal and backgrounds, the Di-Jet mass, or $m(jj)$, has a distribution that would allow to distinguish better signal and backgrounds. This fact is shown in Figures 9.11 and 9.12, where the signal decays slower than in the cases of $H_T$ and $S_T$ for values where the backgrounds are not longer present. This flatter distribution compared to $H_T$ and $S_T$ allows to have a greater number of events outside the regions where the backgrounds are present for the Di-Jet mass variable. It has to be mentioned that these two plots are also for the case where two taus, with the conditions mentioned in the previous paragraph, were required in the event.

A variable that in the normalized plot analysis did not show sepa-

ration between the signal and the background was the transverse mass between the tau and the missing transverse energy. However, looking for other potentially useful varibles for the analysis, the stacked plot $m_T(\tau, \not{E}_T)$ showed good separation between signal and backgrounds. This stacked plot is presented in Figure 9.13, and it can be seen that the signal separates from the background distributions from a value of 300 GeV. However, for the case requiring two taus in the event, the Di-Jet mass would be more useful, because it decays slower than the $m_T$ distribution.

In Figures 9.8, 9.10, 9.12, and 9.13, the distributions for the six heavy neutrinos mass values that were considered in the analysis are shown. Taking into account the discussion presented in Chapter 5, the processes of heavy neutrino production with smaller heavy neutrino mass values have larger cross sections. That is why it would be expected that the distributions mentioned at the beginning of this paragraph should have a larger number of events than the ones that correspond to larger heavy neutrino mass values. However, the signal distributions shown in Figures 9.8, 9.10, 9.12, and 9.13 do not display this behaviour, because in none of these distributions, the signal with 0.1 TeV mass value has the largest number of events. This reduction in the number of events for processes with larger cross section is caused by the selection criteria implemented for the analysis. Most of the particles in the final state of the process come from the decay of the heavy neutrino, so the smaller the mass of the heavy neutrino, the smaller the energy of the particles resulting from the neutrino decay. Since many of the selection criteria established for this analysis are related with the energy of the particle, the number of events that pass the selection criteria decreases when the mass of the heavy neutrino decreases. This is why the signal values that have bigger cross sections do not have greater number of events than the ones with smaller cross sections. Nevertheless, for mass values bigger than 1.0 TeV, the distributions do follow the rule of having more number of events if the cross section is larger.
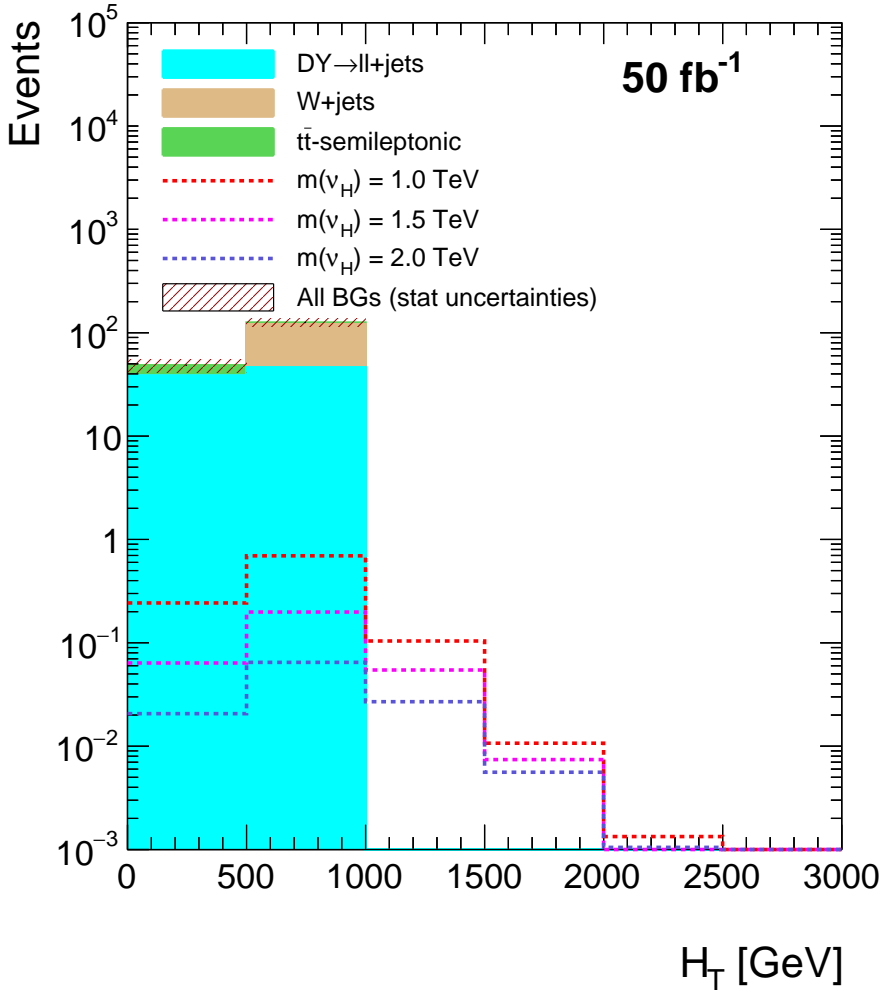
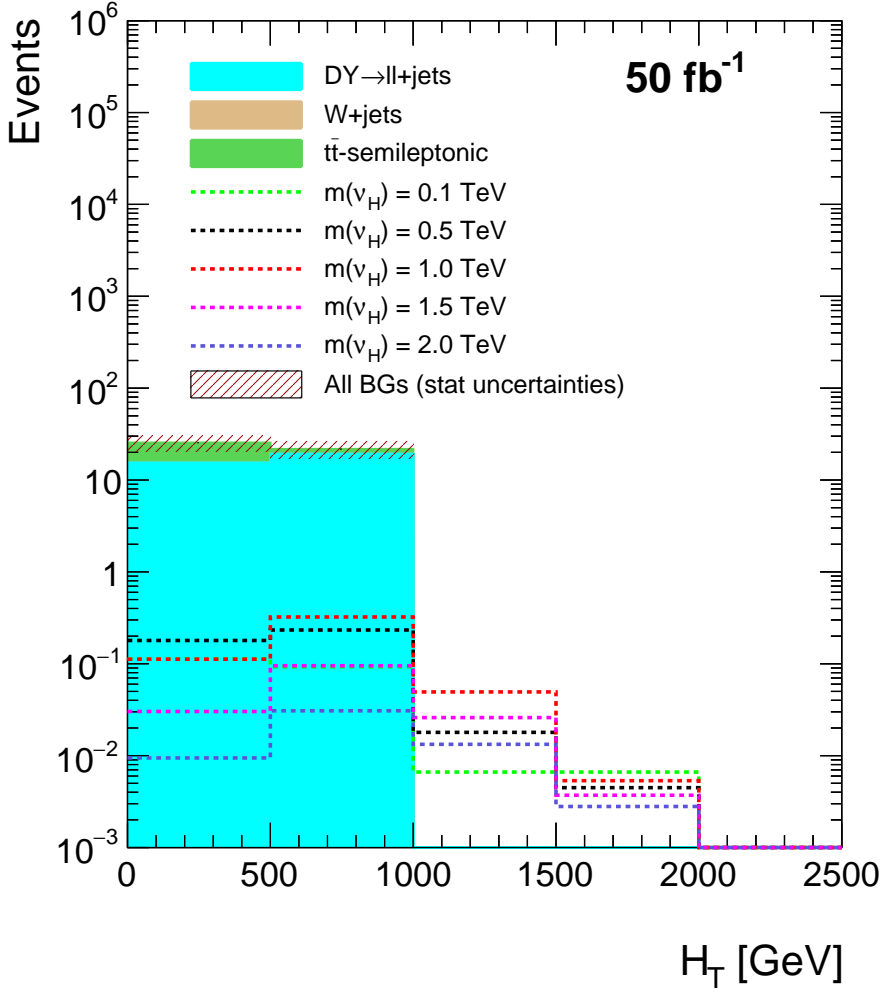Figure 9.7: Stacked plot of $H_T$ requiring two taus in the event and with $\not{E}_T > 50$

Figure 9.8: Stacked plot of $H_T$ requiring two taus in the event and with $\not{E}_T > 60$
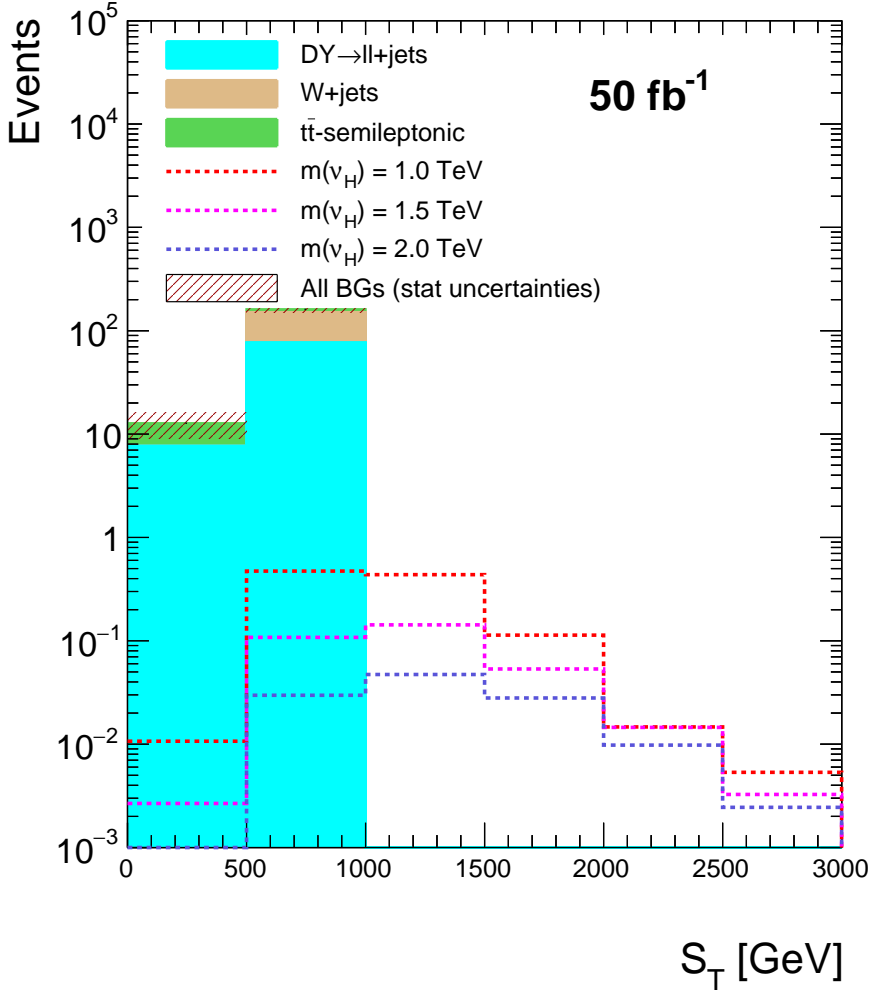
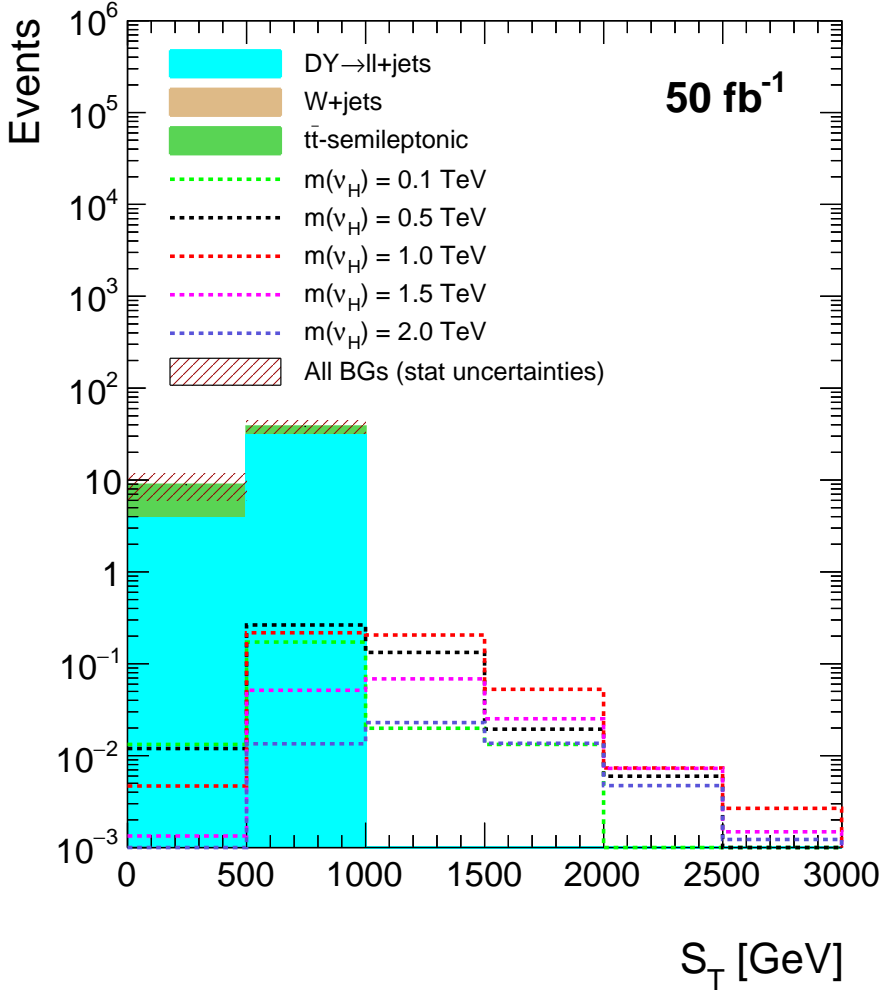Figure 9.9: Stacked plot of $S_T$ requiring two taus in the event and with $\not{E}_T > 50$

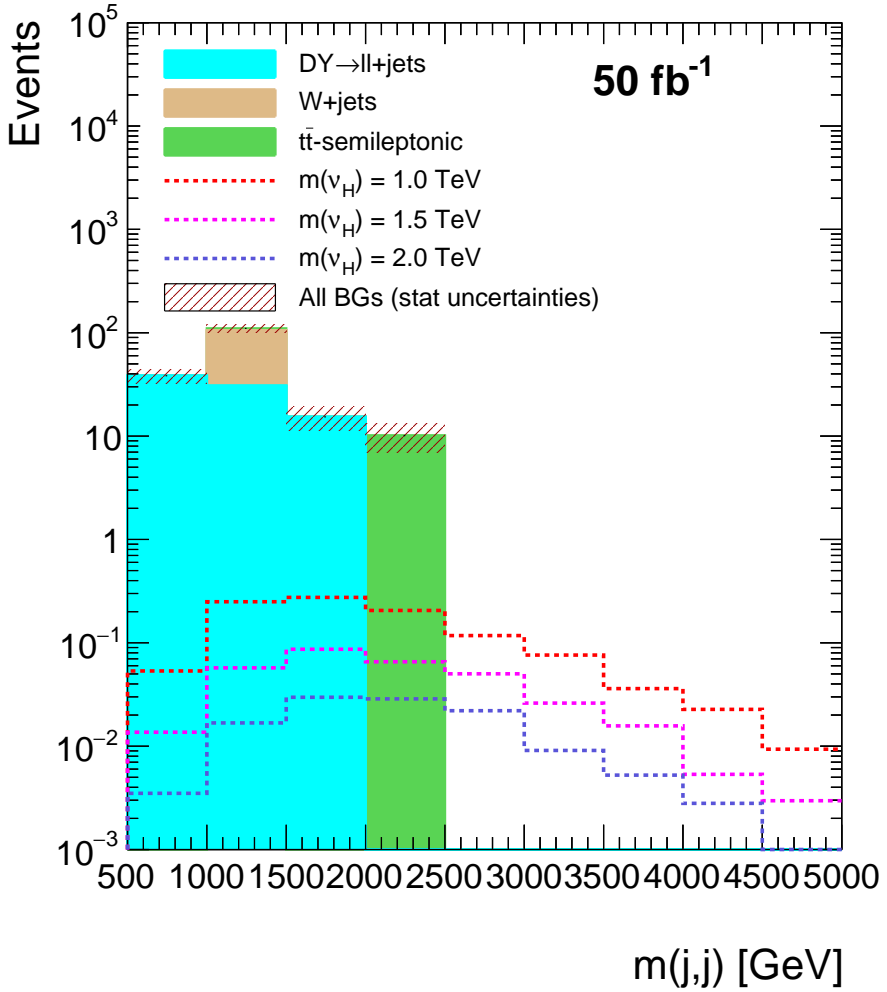Figure 9.10: Stacked plot of $S_T$ requiring two taus in the event and with $\not{E}_T > 60$

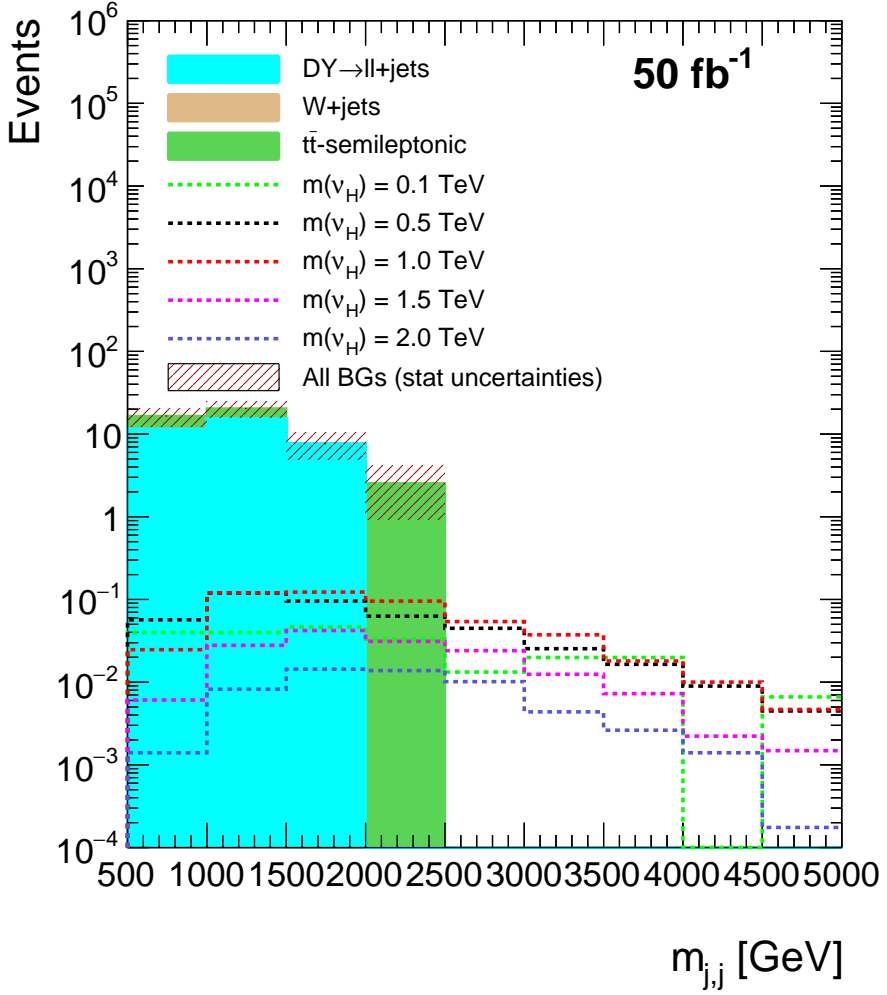Figure 9.11: Stacked plot of Di-Jet mass requiring two taus in the event and with $\not{E}_T > 50$

Figure 9.12: Stacked plot of Di-Jet mass requiring two taus in the event and with $\not{E}_T > 60$
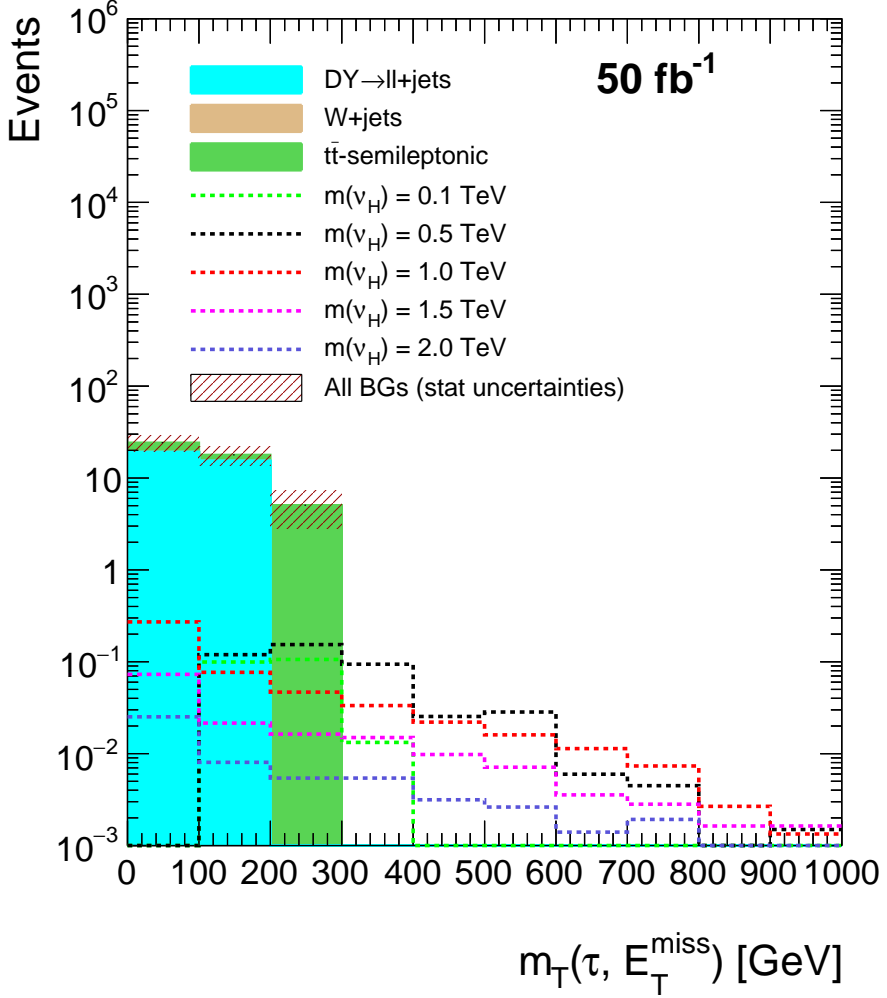
Figure 9.13: Stacked plot $m_T$ between the $\tau$ and the $\not{E}_T$ requiring two taus in the event and with $\not{E}_T > 60$

Besides the case requiring two taus in the event with the selection criteria mentioned previously, the case requiring only one tau with a minimum transverse momentum of 50 GeV was studied. The plots for

this case are shown in Figures 9.14, 9.15, and 9.16. These three plots already include the increase in the $\not{E}_T$ cut discussed at the beginning of this section. In these plots it can be seen that the total amount of background for this case is increased in almost three orders of magnitude. In particular, the W+jets process has significantly more events in the case for one tau after applying all the cuts. However, the dominant background process for both the two taus and one tau cases is the Drell-Yan process.

The main difference between the one tau and two tau case in the relevance of the Di-Jet mass variable. As mentioned earlier, the amount of background increases significantly for the case where only one tau in the event is required. This increase in the background amount affects the separation between signal and backgrounds in $m(jj)$ observed in the case where two taus were required. This fact can be seen in the Di-Jet mass distribution presented in 9.15. This is why the distribution of the transverse mass between the tau and the missing transverse energy was explored. Figure 9.16 shows the distribution of $m_T$ for the case of requiring only one tau. It can be observed that, although a separation as good as the one obtained in $m(jj)$ for the two taus case is not achieved, the $m_T$ distribution has a greater separation between signal and backgrounds than the one in $m(jj)$ in Figure 9.15.
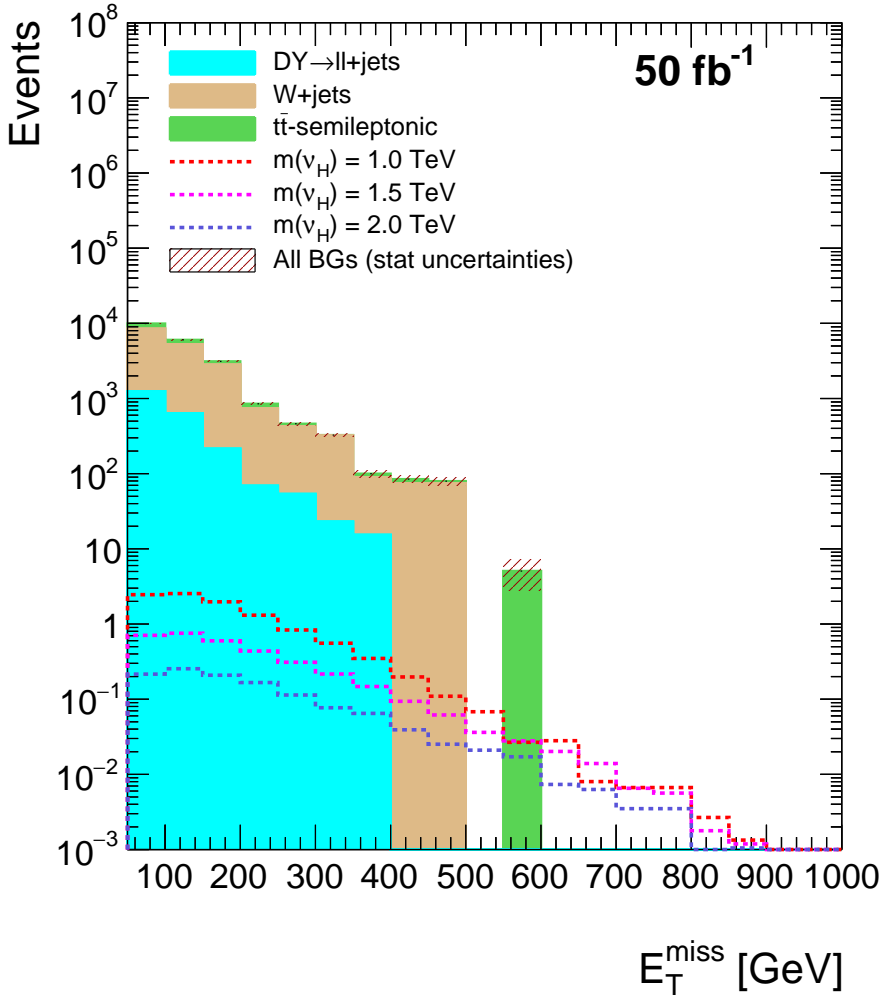
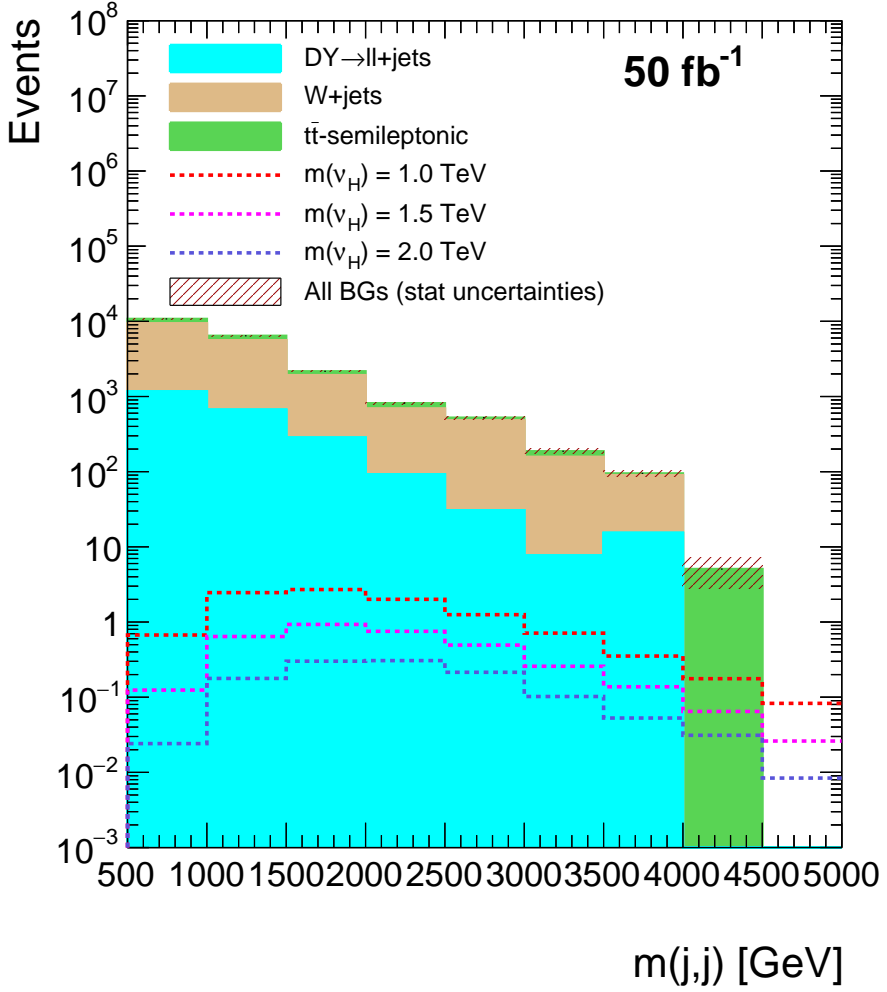Figure 9.14: Stacked plot of $\not{E}_T$ requiring one tau in the event and with $\not{E}_T > 60$

Figure 9.15: Stacked plot of Di-Jet mass requiring only one tau in the event and with $\not{E}_T > 60$

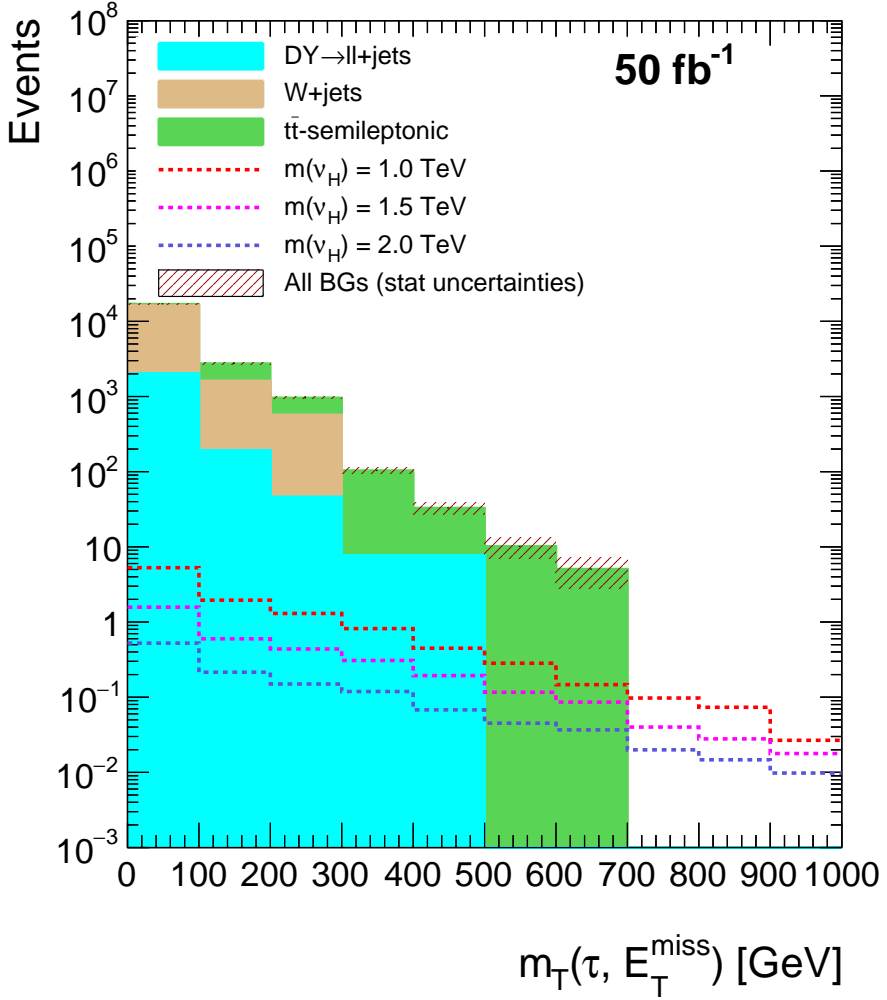Figure 9.16: Stacked plot $m_T$ between the $\tau$ and the $\not{E}_T$ requiring only one tau in the event and with $\not{E}_T > 60$

# Chapter 10

# Summary and Conclusions

In this monograph, a phenomenological analysis seeking to establish whether a search of heavy neutrinos in final states with hadronically decaying tau leptons was feasible to be performed at the LHC, was performed. In the first place, a study of the problem of the neutrino mass was presented in Chapter 4. In this chapter, the reasons for the neutrino not having mass in the SM were presented. Furthermore, the see-saw mechanism, a model that predicts that the SM neutrino has mass and that requires the existance of a heavy right-handed neutrino, was presented. In Chapter 5, a summary of previous heavy neutrino searches in particle experimental physics was given. Also, taking into account the previous heavy neutrino searches, the relevance of the study conducted in this monograph was explained. Moreover, an explanation of the different backgrounds for the heavy neutrino production process considered in this monograph was given in Chapter 6.

For the experimental part, in the first place, the simulations for the different values of the heavy neutrino masses were performed. These simulations included the generation of the process under study using MadGraph, the hadronization using Pythia, and the inclusion of detector effects using Delphes. After these simulations, some preselection criteria, presented in Section 8.1, for particle selection were defined. Also, multiple selection criteria, that could allow the separation between the signal distribution and background, were defined. As presented in Section 8.2, some event selection criteria were defined by optimization using

a figure of merit to estimate the best signal to noise ratio, known as significance. Other selection criteria were defined using physical reasons outlined in Section 8.3. All these selection criteria were implemented in a code using ROOT. Following the selection criteria implementation, the relevant variables for the analysis were selected using normalized to the unit plots. These plots were presented in Section 9.1 and allowed to define $H_T$, $S_T$, and $m(jj)$ as the relevant variables for the analysis. Once the relevant variables were established, the separation between signal and background in these variables had to be studied in more detail using stacked plots. These plots were presented in Section 8.3, and show all the backgrounds distributions and the expected signal separation.

The results obtained in this monograph indicate that a search for heavy neutrinos in final states with hadronically decaying taus, and including the VBF topology, is not feasible. This conclusion can be mainly drawn from the fact that the number of events for either of the six signals analyzed is too small. The selection criteria mentioned in Section 8.3 allow to separate signal from background, so in principle the signal should be detected after performing all the selection criteria. However, it is also true that the number of signal events left after performing all the selection criteria is too small to achieve a considerable experimental sensitivity in the LHC. This small number of events after the cuts can be seen in all the stacked plots presented in Section 9.2. Although the signal distributions indeed separate from the backgrounds in these plots, the amount of signal events that do not overlap with the background are too small. For this reason, and taking into account the results presented in this monograph, a heavy neutrino search, using the VBF production mechanism, would not be feasible in the LHC using the channel with hadronically decaying taus.

# Appendix A

# Same Chirality Fields Terms

A field $\psi$ can be decomposed in its chiral components

$$\psi = \psi_R + \psi_L$$

where

$$\psi_R = \frac{1}{2} \left(1 + \gamma^5\right) \psi \qquad\qquad (A.1)$$

$$\psi_L = \frac{1}{2} \left(1 - \gamma^5\right) \psi \qquad\qquad (A.2)$$

where $\gamma^5$ is the fifth Dirac matrix. Taking into account the Equations A.1 and A.2, the projection operators are defined as

$$P_R = \frac{1}{2} \left(1 + \gamma^5\right)$$

$$P_L = \frac{1}{2} \left(1 - \gamma^5\right)$$

As expected and as shown in Equations A.1 and A.2, $P_R$ projects a field in its right chiral state and $P_L$ projects the field in its left chiral state.

In a similar way the fields $\bar{\psi}_R$ and $\bar{\psi}_L$ are defined as

$$\bar{\psi}_R = \frac{1}{2}\bar{\psi}\left(1 - \gamma^5\right)$$

$$\bar{\psi}_L = \frac{1}{2}\bar{\psi}\left(1 + \gamma^5\right)$$

Taking into account the previous definitions, the term $\bar{\psi}_R \psi_R$ would be

$$\frac{1}{4}\bar{\psi}\left(1 - \gamma^5\right)\left(1 + \gamma^5\right)\psi$$

Remebering the property $\left(\gamma^5\right)^2 = 1$, the term $\left(1 - \gamma^5\right)\left(1 + \gamma^5\right)$ would be zero.

A similar analysis can be performed of the the field with left chirality to obtain the same conclusion. These analysis leads to the conclude that $\bar{\psi}_R \psi_R = \bar{\psi}_L \psi_L = 0$.

# Appendix B

# Mass Eigenstate Majorana Neutrinos Calculation

The eigenvalues of the matrix in Equation 4.16 can be obtained by using the standard method for calculating eigenvalues. That is, the eigenvalues if $\mathcal{M}$ are $\lambda$ values that statisfy

$$\det(\mathcal{M} - \lambda) = 0$$

After some algebra, this determinant is equal to

$$\lambda^2 - \lambda(m_L + m_R) + m_L m_R - m_D^2 = 0$$

Using the quadratic equation to solve for $\lambda$ values, the result is like the one shown in Equation B.1. In this Appendix, the $\lambda$ with the negative sign will be defined as $m_1'$ and the value with the plus sign as $m_2'$.

$$\lambda = \frac{m_R + m_L}{2} \pm \frac{\sqrt{4m_D + (m_R - m_L)^2}}{2} \tag{B.1}$$

Since $\mathcal{M}$ is real and symmetric, a real orthogonal matrix $\mathcal{O}$ that diagonalizes $\mathcal{M}$ exists. In other words, there must by an $\mathcal{O}$ such that the expression in Equation B.2 holds where

$$m_D = \begin{pmatrix} m_1' & 0 \\ 0 & m_2' \end{pmatrix}$$

and

$$\mathcal{O} = \begin{pmatrix} \cos\theta & \sin\theta \\ -\sin\theta & \cos\theta \end{pmatrix}$$

$$\mathcal{O}^\mathsf{T}\mathcal{M}\mathcal{O} = m_D \tag{B.2}$$

Before continuing with the derivation, it is worth noting that the value for $m_1'$ as defined earlier can take negative values. Since the physical masses have to be positive, a new matrix $m_D$ is defined

$$m_D = \begin{pmatrix} m_1\eta_1 & 0 \\ 0 & m_2\eta_2 \end{pmatrix}$$

where $\eta_1 = -1$, $\eta_2 = 1$, and $m_i' = m_i\eta_i$. That way it is assured that the values of the $m_1$ and $m_2$ are positive. This result can also be achieved by multiplying the first column of $\mathcal{O}$ by $i$. The latter is the procedure followed in Chapter 4 to make the mass values positive.

Since $\mathcal{O}$ is the matrix that diagonalizes $\mathcal{M}$, then the field $\nu_L$ is related to $N_L$ by the expression shown Equation B.3 where $N_L$ is the vector with definite mass fields, i.e. the fields with mass $m_1$ and $m_2$ defined as in Equation B.4.

$$\nu_L = \mathcal{O}N_L \tag{B.3}$$

$$N_L = \begin{pmatrix} \nu_1 \\ \nu_2 \end{pmatrix} \tag{B.4}$$

With the definitions presented in Equations B.3 and B.4, the equations shown in 4.17 become clear.

# Bibliography

[1] Particle Data Group, Olive, K. A. et al. (2014) Chin.Phys. C38, 090001

[2] Fukuda, S. et al. (2003) Nuclear Instruments and Methods in Physics Research A 501 (2003) pp. 418–462

[3] Decowski, M. (2016). KamLAND's precision neutrino oscillation measurements. Nuclear Physics B, 908, pp.52-61.

[4] K2K Collaboration: Aliu, E. et al (2005). Evidence for Muon Neutrino Oscillation in an Accelerator-Based Experiment. Physical Review Letters, 94(8).

[5] Nakamura, K. et al. (2010) (Particle Data Group), J. Phys. G 37, 075021 (2010)

[6] Deppisch, F., Bhupal Dev, P., & Pilaftsis, A. (2015). Neutrinos and collider physics. New Journal Of Physics, 17(7), 075019. http://dx.doi.org/10.1088/1367-2630/17/7/075019

[7] Abdesslam, A. et al. (2014) Type II Seesaw Higgsology and LEP/LHC constraints. arXiv:1411.5645 [hep-ph]

[8] Khachatryan, V., Sirunyan, A., Tumasyan, A., Adam, W., Asilar, E., & Bergauer, T. et al. (2016). Search for heavy Majorana neutrinos in $e \pm e \pm$ + jets and $e\pm \mu \pm$ + jets events in proton-proton collisions at s = 8 $\sqrt{s} = 8$ TeV. Journal Of High Energy Physics, 2016(4).

[9] Brooke, J., Buckley, M., Dunne, P., Penning, B., Tamanas, J., & Zgubič, M. (2016). Vector boson fusion searches for dark matter at the LHC. Physical Review D, 93(11). http://dx.doi.org/10.1103/physrevd.93.113013

[10] Ryan Atkin. Review of jet reconstruction algorithms. Journal of Physics: Conference Series, 645(1):012008, 2015

[11] Henley, E., & Garcia, A. (2012). Subatomic physics (1st ed., pp. 206-211). New Jersey: World Scientific.

[12] Kim, C., & Pevsner, A. (1993). Neutrinos in Physics and Astrophysics (1st ed.). Langhorne, PA: Harwood Academic.

[13] Mohapatra, R., & Pal, P. (1991). Massive neutrinos in physics and astrophysics (1st ed., pp. 31-32). Singapore: World Scientific.

[14] Mohapatra, R. (2004). Physics of Neutrino Mass. Lecture, SLAC Summer Institute on Particle Physics.

[15] Almeida, F., Coutinho, Y., Simões, J., & Vale, M. (2000). Signature for heavy Majorana neutrinos in hadronic collisions. Physical Review D, 62(7). http://dx.doi.org/10.1103/physrevd.62.075004

[16] Bray, S., Lee, J., & Pilaftsis, A. (2007). Resonant CP violation due to heavy neutrinos at the LHC. Nuclear Physics B, 786(1-2), 95-118. http://dx.doi.org/10.1016/j.nuclphysb.2007.07.002

[17] Alwall, J., Herquet, M., Maltoni, F., Mattelaer, O., & Stelzer, T. (2011). MadGraph 5: going beyond. Journal Of High Energy Physics, 2011(6). http://dx.doi.org/10.1007/jhep06(2011)128

[18] Sjöstrand, T., Ask, S., Christiansen, J., Corke, R., Desai, N., & Ilten, P. et al. (2015). An introduction to PYTHIA 8.2. Computer Physics Communications, 191, 159-177. http://dx.doi.org/10.1016/j.cpc.2015.01.024

[19] de Favereau, J., Delaere, C., Demin, P., Giammanco, A., Lemaître, V., Mertens, A., & Selvaggi, M. (2014). DELPHES

3: a modular framework for fast simulation of a generic collider experiment. Journal Of High Energy Physics, 2014(2). http://dx.doi.org/10.1007/jhep02(2014)057

[20] Antcheva, I., Ballintijn, M., Bellenot, B., Biskup, M., Brun, R., & Buncic, N. et al. (2009). ROOT — A C++ framework for petabyte data storage, statistical analysis and visualization.